RNase L-mediated RNA decay alters 3' end formation and splicing of host mRNAs

James M. Burke[1,8], Nina Ripin[1,2,8], Max B. Ferretti[7], Laura A. St Clair[4,5], Emma R. Worden-Sapper[3], Sara L. Sawyer[3], Rushika Perera[4,5], Kristen W. Lynch[7], and Roy Parker[1,2,6*]

1. Department of Biochemistry, University of Colorado Boulder, Boulder, Colorado, 80303
2. Howard Hughes Medical Institute, University of Colorado Boulder, Boulder, Colorado, 80303
3.Department of Molecular, Cellular and Developmental Biology, University of Colorado Boulder, Boulder, CO 80309, USA.
4. Center for Vector-Borne and Infectious Diseases, Department of Microbiology, Immunology and Pathology, Colorado State University, Fort Collins, CO 80523, USA.
5. Center for Metabolism of Infectious Diseases, Colorado State University, Fort Collins, CO 80523, USA.
6. BioFrontiers Institute, University of Colorado Boulder, Boulder, Colorado, 80303
7. Department of Biochemistry and Biophysics, Perelman School of Medicine, University of Pennsylvania, Philadelphia, PA, USA
8. Authors contributed equally.

***Correspondence:** roy.parker@colorado.edu

ABSTRACT

The antiviral endoribonuclease, RNase L, is a vital component of the mammalian innate immune response that destroys host and viral RNA to reduce viral gene expression. Herein, we show that a consequence of RNase L-mediated decay of cytoplasmic host RNAs is the widespread re-localization of RNA-binding proteins (RBPs) from the cytoplasm to the nucleus, due to the presence of nuclear RNA. Concurrently, we observe global alterations to host RNA processing in the nucleus, including alterations of splicing and 3' end formation, with the latter leading to downstream of gene (DoG) transcripts. While affecting many host mRNAs, these alterations are pronounced in mRNAs encoding type I and type III interferons and coincide with the retention of their mRNAs in the nucleus. Similar RNA processing defects also occur during infection with either dengue virus or SARS-CoV-2 when RNase L is activated. These findings reveal that the distribution of RBPs between the nucleus and cytosol is fundamentally dictated by the availability of RNA in each compartment and thus viral infections that trigger cytoplasmic RNA degradation alter RNA processing due to the nuclear influx of RNA binding proteins.

40 **INTRODUCTION**

41

42 Ribonuclease L (RNase L) limits the replication of diverse viruses, including influenza virus,
43 chikungunya virus, SARS-CoV-2, and vaccinia virus (Min and Krug, 2006; Cooper et al., 2015; Li et al.,
44 2016; Li et al., 2021). RNase L is activated by 2'-5'-oligo(A), which is produced by 2'-5'-oligoadenylate
45 synthetases (OASs) upon binding to viral or endogenous dsRNA (reviewed in Silverman, 2007; Kristiansen
46 et al., 2011). RNase L cleaves at UN^N motifs in single-stranded RNA (ssRNA) regions (Floyd-Smith et
47 al., 198l; Wreschner et al., 1981), and destruction of viral RNAs by RNase L reduces viral replication (Han
48 et al., 2007; Cooper et al., 2015, Nogimori et al., 2019; Burke et al., 2021b.). In addition, RNase L also
49 cleaves several types of cellular RNAs, including rRNAs, tRNAs, and mRNAs (Wreschner et al., 1981;
50 Andersen et al, 2009; Donovan et al., 2017; Rath et al., 2019; Burke et al, 2019).

51

52 We, and others, recently demonstrated that RNase L activation results in widespread degradation
53 of most host basal mRNAs (Burke et al., 2019; Rath et al., 2019). This has several impacts to cellular RNA
54 biology. First, it allows for antiviral programming of translation since several immediate early antiviral
55 mRNAs (i.e., *interferon* mRNAs) escape RNase L-mediated mRNA decay. Second, it inhibits the assembly
56 of stress granules (Burke et al., 2020), cytoplasmic ribonucleoprotein (RNP) complexes proposed to
57 modulate aspects of the antiviral response (Onomoto et al., 2012; Reineke and Lloyd, 2014; Yoo et al.,
58 2014). Third, it promotes the formation of an alternative cytoplasmic RNP granule of unknown function
59 termed RNase L-dependent bodies (RLBs) (Burke et al., 2020). Fourth, it inhibits nuclear mRNA export,
60 which substantially reduces protein production of influenza virus as well as host cytokines induced by
61 dsRNA, dengue virus infection, or SARS-CoV-2 infection (Burke et al., 2021a, Burke et al., 2021b). Lastly,
62 it results in the translocation of poly(A)-binding protein (PABP) from the cytoplasm to the nucleus (Burke
63 et al., 2019).

64

65 Herein, we demonstrate that RNase L-mediated degradation of host mRNAs primarily occurs in
66 the cytoplasm, which leads to the re-localization of many RBPs to the nucleus in a manner dependent on
67 intact nuclear RNA. This demonstrates the fundamental principle that the distribution of RBPs between
68 subcellular compartments is dependent on the availability of their binding sites. The influx of RBPs into
69 the nucleus is concurrent with global RNase L-dependent RNA processing alterations including alternative
70 splicing, intron retention and transcription read-through leading to downstream of gene (DoG) transcript
71 production, both of which correlate with inhibition of nuclear export of *IFN* mRNAs. These are general
72 responses since we observe these alterations in RNA processing occur during exposure to exogenous
73 dsRNA, dengue virus serotype 2 (DENV2) infection, or severe acute respiratory syndrome coronavirus 2

74 (SARS-CoV-2) infection. These findings show that RNase L-mediated mRNA decay alters the balance of
75 RNA-binding protein subcellular localization, host RNA processing events, and antiviral gene expression.
76 Since RBPs can also regulate transcription (Xiao et al., 2019), this work strongly implies that widespread
77 RNA degradation in the cytosol will also lead to changes in transcription of multiple genes.

RESULTS

RNase L activation triggers re-localization of multiple RNA-binding proteins to the nucleus

The poly(A)-binding protein (PABP) primarily localizes to the cytoplasm in unstressed A549 cells (Figure 1A). However, upon lipofection of poly(I:C), PABP translocates to the nucleus (Fig. 1A & Burke et al., 2019). The translocation of PABP to the nucleus in response to poly(I:C) is dependent on RNase L since it does not occur in RNase L-KO A549 cells (Fig. 1A) but is rescued in RNase L-KO cells upon restoration of RNase L expression (Burke et al., 2019).

To determine if RNase L activation led to the import of additional RNA-binding proteins (RBPs), we performed immunofluorescence assays for several RBPs in WT and RL-KO cells post-poly(I:C) lipofection. A striking result is that RNase L activation promotes the nuclear localization of several RBPs (Fig. 1B,C), including CUGBP-1, FAM120A, TIA-1, Caprin-1, pumilio, and Ataxin-2, although some RBPs, such as G3BP1 and FMRP, only showed small, but significant, increases (Fig. 1B,C). These data indicate that RNase L activation results in the accumulation of RBPs in the nucleus.

RNase L and RNase L-mediated RNA decay are primarily localized to the cytoplasm

One mechanism by which RNase L could alter the localization of RBPs between the nucleus and cytoplasm is differential RNA degradation between the cytoplasm and nucleus, whereby higher RNA decay in the cytoplasm relative to the nucleus would lead to disassociation of RBPs from cytoplasmic RNA more rapidly than from nuclear RNA. To assess this, we quantified poly(A)+ RNA in the cytoplasm and nucleus of WT and RL-KO cells lipofected with or without post-poly(I:C) (Fig. 2A). We also stained cells for G3BP1 to identify cells undergoing a dsRNA response, whereby WT cells with activated RNase L contain RNase L-dependent bodies (RLBs) or RL-KO cells with activated PKR contain stress granules (SGs) (Burke et al., 2020).

Importantly, we did not observe a significant reduction of poly(A)+ RNA staining in the nucleus of RLB-positive WT cells (Fig. 2A,B), whereas poly(A)+ RNA was significantly reduced in the cytoplasm (Fig. 2A,B). Moreover, we did not observe reduced cytoplasmic poly(A)+ RNA staining in SG-positive RL-KO cells. Consistent with these observations, the *GAPDH* mRNA accumulates in the nucleus while being degraded in the cytoplasm when RNase L is activated (Burke et al., 2021a). These data indicate that RNase L-mediated RNA decay primarily occurs in the cytoplasm in A549 cells.

While previous studies have shown that RNase L can localize to both the cytoplasm and nucleus (Bayard and Gabrion, 1993; Al-Ahmadi et al., 2009), we observed that endogenous RNase L is almost exclusively localized to the cytoplasm in A549 cells via cellular fractionation followed by immunoblot analysis (Fig. 2C). Combined, these data indicate that RNase L-mediated RNA decay primarily occurs in the cytoplasm.

Nuclear influx of RBPs is dependent on nuclear RNA

In principle, RNase L activation could alter RBP localization in two manners. First, RBPs may be subject to post-translational modifications, indirectly promoted by RNase L activation, that increase their nuclear accumulation. Alternatively, free RBPs may shuttle between the nucleus and cytosol faster that RBPs bound to RNA, and therefore the degradation of bulk cytoplasmic RNA would allow RBPs to shuttle to the nucleus, where binding to nuclear RNA would retain the RBPs in the nucleus. A prediction of this latter model is that the accumulation of nuclear RBPs will be dependent on the presence of a pool of nuclear RNA to bind the RBPs and increase their dwell time in the nucleus (Fig. 2D).

To test whether nuclear RNA is required for PABP accumulation in the nucleus, we assayed PABP localization when nuclear RNAs are degraded concurrently with cytoplasmic RNAs in response to RNase L activation (Fig 2D). To do this, we used A549 cells that constitutively express RNase L tagged with a nuclear localization signal (NLS) that we previously generated and termed NLS-RNase L (Decker et al., 2021). Unlike RNase L, which strictly localizes to the cytoplasm (Fig. 2C), the RL-NLS localizes to both the cytosol and nucleus (Fig. 2E) and degrades nuclear RNAs in response to poly(I:C) lipofection (Decker et al., 2021). We examined PABP localization via immunofluorescence and RNA levels via poly(dT) FISH post-poly(I:C) lipofection.

An important result is that RNase L-mediated degradation of both nuclear and cytoplasmic RNA reduced the accumulation of PABP in the nucleus. Specifically, in cells where RNase L is targeted to the nucleus (A549-NLS-RL), we observed a reduction in poly(A)+ RNA staining in both the nucleus and cytoplasm following poly(I:C) lipofection in comparison to mock-treated A549 cells (Fig. 2F,G). Importantly, PABP remained predominately localized to the cytoplasm in A549-NLS-RL cells in which RNase L degraded both cytoplasmic and nuclear RNAs (Fig. 2,F,G). In contrast, transfection of poly(I:C) in A549 cells only reduced cytoplasmic poly(A)+ RNA, not nuclear poly(A)+ RNA in comparison to mock

145 treated cells (Fig. 2F,G). In these cells, PABP staining increased in the nucleus and decreased in the
146 cytoplasm in comparison to mock-treated cells (Fig. 2F,G).
147
148 These data demonstrate that RNase L activation increases the nuclear localization of several RBPs
149 by increasing the relative number of RBP-binding sites in the nucleus relative to the cytoplasm as a result
150 of degradation of cytoplasmic but not nuclear mRNAs.
151
152 **RNase L alters host mRNA processing**
153
154 The above data imply that RBPs translocated to the nucleus upon RNase L activation associate with
155 RNA. This influx of RBPs would be predicted to compete for RNA-binding with RBPs involved in mRNA
156 processing and thereby alter nuclear RNA processing. To examine if RNase L activation alters RNA
157 processing, we analyzed high-throughput RNA sequencing (RNA-seq) of WT and RL-KO cells following
158 six hours of either mock treatment or poly(I:C) lipofection (Burke et al., 2019).
159
160 To examine if there were changes to alternative splicing, we utilized MAJIQ (see methods) which
161 identifies changes in alternative splicing patterns. Splicing changes are expressed for a given splicing event
162 as the Percentage Spliced In (PSI). Thus, we compared the PSI of splicing events between WT or RL KO
163 cells treated with or without poly(I:C) to identify changes in RNA splicing that occur in response to dsRNA
164 and that are dependent on RNase L.
165
166 This analysis identified 140 splicing events, across 136 genes, that showed differential splicing
167 either due to poly(I:C) treatment in the WT cells, or were different between the WT and RL KO cell lines
168 post-poly(I:C). These changes are calculated as the difference in PSI between two conditions, the ΔPSI.
169 The changes in splicing in both cases were generally correlated, which indicates that the majority of changes
170 in alternative splicing observed are due to activation of RNase L (Figure 3A). Splicing alteration in 60
171 genes were statistically significant under both comparisons (Figure 3B). Strikingly, 14 of these 60 genes
172 encode RBPs involved in pre-mRNA splicing. This is notable since many RBPs autoregulate their own
173 splicing (Muller-McNicoll et al., 2019), and this would be consistent with increased nuclear occupancy of
174 RBPs following activation of RNase L.
175
176 To validate the analysis of RNA-Seq data, we prepared RNA from mock and poly(I:C) treated WT
177 and RL-KO cells and examined a subset of splicing events by low cycle radiolabeled RT-PCR. In all four
178 cases examined (TMEM69, IPO9, PTBP1, and SRSF2), we observed a changed in exon inclusion with

179 poly(I:C) treatment that was dependent on RNase L (Figure 3C). This demonstrates that RNase L activation
180 can lead to changes in alternative splicing patterns.
181
182 Another alteration of splicing can be overall decreased splicing rates and the increased retention of
183 introns (intron retention (IR)). To determine if intron retention is affected by RNase L activation, we
184 calculated an intron/exon ratio (TPM normalized intron over TPM normalized exon counts) per RNA for
185 WT and RL-KO cells with or without poly(I:C) transfection. An increase in intron retention correlates with
186 an increase in the intron/exon ratio.
187
188 A striking result was that density plots of all RNAs showed a shift to higher intron/exon ratios upon
189 poly(I:C) treatment in WT cells, highlighting an RNase L-dependent increase in IR (Fig. 4A). The same
190 shift was also observed for transcripts that are either unchanged (Fig. S1A), downregulated (Fig. S1C) or
191 upregulated (Fig. S1E) in WT cells upon poly(I:C) treatment. Consistent with these analyses, IGV traces
192 of multiple example genes displayed increased reads mapping to introns (Fig. 4B, S2B,D,F).
193
194 We note that for upregulated genes, a shift towards higher intron/exon ratio is visible in wild-type
195 cells compared to RL-KO cells, consistent with an increase in intron retention. However, an additional shift
196 is also visible in both unstressed conditions (Fig. S2C). This is caused by multiple factors. First, a few genes
197 showed high intron retention in RL-KO cells even without stress. Second, transcriptional read-through from
198 upstream genes (see below), causes increased ratios. The majority of such transcripts is filtered out by initial
199 filtering steps (material and methods), however, especially for upregulated genes, some transcripts remain
200 and can cause false positive increased ratios. Third, wrong gene annotations (e.g. an exon with increased
201 reads is counted within intronic region), can make increase in ratio for upregulated genes more pronounced.
202 And lastly, despite an overall increase in IR in WT cells upon poly(I:C) (Fig. S1F), the intron/exon ratio
203 decreases due to the increased expression and higher exon counts over the intron counts, especially for
204 genes with short introns and large exons.
205
206 These data argue that RNase L activation also decreases the efficiency of intron removal, which is
207 supported by smFISH data of selected targets (see below).
208
209 We also observed that RNase L activation perturbs transcription termination. Specifically, we
210 examined whether RNase L activation resulted in downstream of gene (DoG) transcriptional read-through,
211 which are observed during viral infection and various other stresses and are consistent with defects in
212 transcription termination (Vilborg and Steitz, 2017; Vilborg et al., 2015; Rutkowski et al., 2015; Bauer et

213 al., 2018). To do this, we calculated an $DoG_{1\text{-}5000}$/exon ratio, where $DoG_{1\text{-}5000}$ corresponds to TPM
214 normalized counts over the first 5000 nt after the annotated gene end (Fig. 4B and Fig. S2A,C,D) (see
215 methods).
216
217 In WT cells transfected with poly(I:C), we observed DoG transcripts, which were notably absent
218 in poly(I:C)-transfected RL-KO cells (Fig. 4B,C). For example, IGV traces for multiple RNAs demonstrates
219 increased reads mapping to the DoG region in WT cells treated with poly(I:C) that are absent in mock-
220 treated WT or RL-KO cells as well as poly(I:C)-treated RL-KO cells (Fig. 4C and Fig. S2,B,D,F).
221
222 We confirmed DoG formation in the long non-coding RNA, NORAD, using two smFISH probes,
223 with one targeting the NORAD RNA region and a second targeting the DoG region of NORAD (Fig. S3A).
224 Staining cells twelve hours post-poly(I:C) lipofection revealed accumulation of RNAs with 3' DoGs as
225 detected by hybridization to the probe downstream of the NORAD coding region in WT but not RL-KO
226 cells (Fig. S3B). Consistent with earlier results, we also observed RNase L-mediated degradation of the
227 cytosolic NORAD RNA (Burke et al., 2019), and the accumulation of NORAD RNA in the nucleus due to
228 a block to nuclear export (Burke et al., 2021). As expected, in the RL-KO cells, cytosolic NORAD RNA
229 was not degraded and accumulated in stress granules (Khong et al., 2017). DoG RNAs co-localized with
230 NORAD RNA at both the site of transcription (2 large/intense foci) as well as dispersed in the nucleus as
231 individual RNAs (Fig. S3B).
232
233 These observations indicate that RNase L activation results in global nuclear RNA processing
234 alterations, including changes in alternative splicing, intron retention and reduced transcription termination.
235
236 **RNase L activation alters antiviral mRNA biogenesis**
237
238 A key aspect of the cellular response to dsRNA is the induction of antiviral gene expression. Given
239 this, we examined how RNase L activity affected the processing of mRNAs transcriptionally induced by
240 dsRNA, including type I and type III interferons (IFNs). We observed that RNase L altered the RNA
241 processing of the pre-mRNAs for both types of interferons. For example, we observed increased RNA-seq
242 reads mapping downstream of *IFNB1* and *IFNL1* in WT cells in comparison to RL-KO cells (Fig. 5A,B),
243 indicating downstream of gene (DoG) transcriptional read-through when RNase L is activated. Moreover,
244 we observed increased reads mapping to the introns of IFNL1, indicative of intron retention (Fig. 5B). To
245 validate these data, we performed smFISH using probes that target the DoG of IFNB1 and IFNL1 or the
246 introns of IFNL1.

247

248 Consistent with our RNA-seq analyses, several observations indicate that RNase L promotes
249 transcriptional read-through of *IFNL1* and *IFNB1* genes. First, in a portion of WT cells that induced IFNB1
250 or IFNL1 expression in response to poly(I:C), as determined by co-smFISH for the CDS regions of these
251 genes (Fig. S4A,B,C,D,E), we observed abundant and disseminated DoG smFISH foci (Fig. 5B,C,D). We
252 note that we did not observe abundant smFISH foci targeting the DoG-2 region, which is further
253 downstream of the DoG 1 region of IFNB in WT cells (Fig S5A). This correlates with lower reads mapping
254 to this region and consistent with lower abundance of these transcripts as assessed by RNA-seq. We did
255 observe staining for the DoG-2 region of IFNL1, but note that it was predominantly localized to the sites
256 of transcription (Fig. S5B).

257

258 *IFNB1* and *IFNL1* DoG RNA staining was significantly less abundant in RL-KO cells in
259 comparison to WT cells despite RL-KO cells containing higher levels of CDS staining for both IFNB1 and
260 IFNL1 (Fig. S4A,B,C,D). Notably, IFNB1-DoG staining was mostly confined to large foci that are
261 consistent with IFNB1 sites of transcription in RL-KO cell (Fig. 5C), and the IFNL1-DoG RNA was not
262 observed in RL-KO cells (Fig. 5D). These data demonstrate that that RNase L promotes DoG read-through
263 transcription of *IFNB1* and *IFNL1* genes.

264

265 *IFNL1* intron staining was largely observed at sites consistent with the IFNL1 sites of transcription,
266 and this was observed in both WT and RNase L-KO cells (Fig. 5E). Nevertheless, we observed increased
267 IFNL1-intron smFISH foci in WT cells in comparison to RL-KO cells (Fig. 5E). This observation is
268 consistent with the RNA-seq data and demonstrates that RNase L activation promotes intron retention in
269 *IFNL* transcripts.

270

271 **Alterations in RNA processing contribute to nuclear retention of antiviral mRNAs**

272

273 We have previously documented that RNase L activation can lead to nuclear retention of host and
274 viral mRNAs (Burke et al., 2021a). The observation that IFNB1 and IFNL1 DoG RNAs are largely
275 localized to the nucleus led us to examine whether DoG RNA included on the IFNB1 or IFNL1 transcripts
276 could contribute to their nuclear retention. To examine this, we analyzed the localization of DoG RNA and
277 CDS RNA in WT and RL-KO cells following poly(I:C) lipofection.

278

279 Several observations indicate that DoG production from the IFNB1 mRNA contributes to its
280 nuclear retention. First, the IFNB1-DoG RNAs are almost exclusively localized in the nucleus, even in cells

281 that have exported IFNB mRNAs that only stain for the CDS region to the cytosol (Fig. 6A,B; red arrows).
282 Second, in WT cells with abundant and disseminated IFNB1-DoG foci, the DoG foci co-localize with
283 IFNB1-CDS foci that are retained in the nucleus (Fig. 6A; red arrows). Third, IFNB1-CDS foci located in
284 the cytoplasm only contain DoGs in very rare cases (Fig. 6A; red arrows). Lastly, we observed that the
285 abundance of DoG foci positively correlates with the ratio (nuclear/total) of IFNB-CDS or the absolute
286 number of nuclear IFNB-CDS foci (Fig. 6C,D). We observed similar effects eight hours post-transfection
287 with poly (I:C) (Fig. S6A,B,C,D,E). These data argue that IFNB1 RNA transcripts containing the DoG
288 RNA are not exported to the cytoplasm and argue that DoG formation contributes to the inhibition of export
289 of IFNB mRNAs.
290
291 Our data suggests that additional mechanisms can inhibit mRNA export. For IFNB mRNA, we
292 also observed cells in which most nuclear-retained IFNB1-CDS RNAs did not contain IFNB-DoG RNA
293 (Fig. 6A, yellow arrow). The accumulation of IFNB mRNAs in the nucleus that do not hybridize to DoG
294 probes suggests two possibilities. First, there could be a mechanism independent of DoG transcriptional
295 read-through that inhibits *IFNB1* mRNA export, which is supported by our analysis of IFNL1 mRNA (see
296 below). However, we cannot rule out the formal possibility that all the nuclear retained IFNB RNAs could
297 contain DoGs, but with some being too short to hybridize to the DoG probes. However, since the vast
298 majority of RNA-seq reads end at the normal 3' end of IFNB mRNAs (Fig. 5A), we consider this possibility
299 unlikely.
300
301 The examination of IFNL1 mRNAs provides additional evidence for a block to mRNA export that
302 is independent of RNA processing defects. Specifically, we observed that most of the nuclear-retained
303 IFNL1 mRNA did not hybridize to smFISH probes for IFN1L introns or DoGs and were much more
304 abundant than the DoG and intron foci (Fig. 6E,F,G). We note that we did observe that IFN1L mRNAs
305 that contained DoGs or intron sequences were mostly nuclear-retained (Fig. 6E,H), consistent with defects
306 in RNA processing limiting RNA export.
307
308 Taken together, these observations demonstrate the defects in RNA processing can contribute to
309 nuclear retention of mRNAs after RNase L activation, but also provide evidence for a block to mRNA
310 export independent of DoG-RNA inclusion and intron retention.
311
312 **Re-localization of RBPs and RNA processing alterations occur during viral infection**
313

314 One limitation of the above experiments is that we have used poly(I:C) as a dsRNA mimic of viral
315 infection. In order to verify that these alterations were relevant to viral infection, we examined whether
316 RNase L-dependent re-localization of RBPs and nuclear RNA processing alterations occurred during viral
317 infection. We analyzed PABP localization via immunofluorescence in WT and RL-KO A549 cells
318 following infection with either dengue virus serotype 2 (DENV2) or SARS-CoV-2 (using $A549^{ACE2}$ cells),
319 both of which activate RNase L (Burke et al., 2021a; Burke et al., 2021b; Li et al., 2021). To identify
320 infected cells, we co-stained the viral mRNAs via single-molecule fluorescence in situ hybridization
321 (smFISH), while alterations in RNA processing were examined by smFISH for IFNB of IFN1L DoGs or
322 introns.
323
324 These analyses showed that RNase L activation promotes PABP translocation to the nucleus and
325 alteration of RNA processing in response to SARS-CoV-2 infection (Fig. 7A,B,C,D,E). Specifically, all
326 WT A549 cells infected with SARS-CoV-2, as detected by smFISH for the viral RNA, displayed
327 accumulation of PABP in the nucleus (Figure 7A; white arrows), which was not observed in RL-KO cells.
328 Moreover, smFISH for IFNB1 CDS and DoG demonstrated the production of IFNB1 DoGs during SARS-
329 CoV-2 infection was higher in WT but not RL-KO cells (Fig. 7 D,E). Notably, IFNB1 transcripts containing
330 DoG RNAs were largely localized in the nucleus (Fig. 7D).
331
332 Similar results were observed with DENV-infected cells, although approximately half of DENV-
333 infected cells do not activate RNase L-mediated mRNA decay (Burke et al., 2021a) (Fig. S7A). Thus,
334 approximately half of DENV-infected cells did not display translocation of PABP to the nucleus as expected
335 (Fig. 8A and Fig. S7B). However, we observed many DENV2-infected WT cells assembled RLBs, whereas
336 many DENV2-infected RL-KO cells assembled SGs (Fig. 8A). This allowed us to identify cells that
337 activated the dsRNA immune response. We then calculated the nuclear to cytoplasmic PABP in DENV-
338 infected WT cells that activated RNase L (RLB+) or RL-KO cells that activated PKR (SG+) in comparison
339 to cells that did not activate dsRNA response (RL- for WT cells or SG- for RL-KO cells). These analyses
340 revealed a substantial increase in nuclear PABP specifically in DENV2-infected WT cells that activated
341 RNase L (Fig. 8B,C).
342
343 Examination of RNA processing defects in DENV-infected cells via smFISH revealed that RNase
344 L-dependent RNA processing alterations occurred during these infections. Specifically, we observed that
345 IFNL1-intron and IFNB1-DoG were both higher in DENV-infected WT cells comparison to RL-KO cells
346 (Fig. 8D,E,F).
347

348 Taken together, the analysis of IFN mRNAs documents that RNase L activation either due to
349 poly(I:C) transfection or viral infection triggers the accumulation of RBPs in the nucleus and affects nuclear
350 RNA processing of antiviral mRNAs, with a stronger effect on transcriptional termination leading to the
351 production of DoGs for these mRNAs.

352 **DISCUSSION**

353

354 Several observations support that RNase L-mediated RNA decay results in re-localization of RBPs
355 from the cytoplasm to the nucleus, which in turn alters nuclear RNA processing (Fig. 9). First, we observed
356 that several RBPs concentrate in the nucleus following RNase L activation (Fig. 1A,B). Second, RNase L
357 and RNase L-mediated RNA decay are localized the cytoplasm (Fig. 2A,B,C), sparing nuclear RNA from
358 degradation. Moreover, intact nuclear RNA is required for the accumulation of RBPs to the nucleus,
359 suggesting RBPs associate with nuclear RNA upon influx into the nucleus (Fig. 2E,F,G). Third, our RNA-
360 seq analyses show that RNase L activation triggers global alterations in splicing and transcription
361 termination (Figs. 3 and 4). Fourth, our smFISH analyses show that the number of DoGs and introns are
362 increased in WT cells in comparison to RL-KO cells in response to poly(I:C) lipofection, and that these
363 RNAs can be retained at the sites of transcription or disseminated in the nucleus (Fig. 5C,D,E, Fig. 6A,E,
364 Fig. S3,B). Importantly, we show that RNase L-dependent RBP re-localization to the nucleus and
365 alterations to type I and type III interferon mRNA biogenesis occur during dengue virus or SARS-CoV-2
366 infection (Figs. 7 and 8).

367

368 This work highlights the fundamental conclusion that the availability of RNA-binding sites can
369 influence the distribution of RBPs between the cytosol and nucleus, which explains multiple observations
370 in the literature. First, during the integrated stress response, the release of mRNAs from ribosomes due to
371 phosphorylation of eIF2α exposes new RNA-binding sites for RBPs in the cytoplasm, which causes nuclear
372 RBPs to re-distribute to the cytoplasm and/or stress granules (Fig. 1C, CUGBP1 and TIA-1) (Kedersha et
373 al., 1999). Similarly, the export of RBPs from the nucleus in response to actinomycin D-mediated inhibition
374 of transcription can be understood as a loss of nuclear RNA leading RBPs to associate with cytosolic RNA
375 (Cáceres et al., 1998). Finally, when cytosolic RNAs are degraded by the KSHV viral Sox2 nuclease,
376 numerous RBPs are observed to accumulate in the nucleus (Gilbertson et al., 2018). Thus, sub-cellular
377 changes in RNA abundance and/or availability of RNA binding sites dictates RBP localization for many
378 RBPs. Indeed, a number of RBPs known to act in mRNA processing are themselves differentially spliced
379 upon exposure to poly(I:C) in an RNase L-dependent manner (Fig 3). Interestingly, some RBPs are less
380 affected by cytosolic RNA decay with respect to their localization. For example, G3BP1 shows only a small
381 increase in nuclear accumulation following RNase L activation (Fig. 1B,C). We suspect that this is due to
382 their association with protein substrates that regulate their localization, or a slower intrinsic rate of protein
383 import into the nucleus.

384

385 RNase L-mediated regulation of RBP localization represents a new and important potential
386 antiviral mechanism since studies have shown that host RBPs interact with and can affect viral replication
387 (Li and Nagy, 2011). Since viruses replicate specifically in either the nucleus or cytoplasm, the RNase L-
388 mediated re-localization of RBPs between the cytoplasm and nucleus may promote the antiviral function
389 of RBPs and/or viruses may use RNA decay to avoid host RBPs. Notably, several viruses, including
390 Kaposi's sarcoma-associated herpesvirus (KSHV) and herpes simplex virus 1 (HSV-1) encode for proteins
391 (SOX, VHS, respectively) that degrade cellular RNAs, inhibit nuclear mRNA export, and cause nuclear
392 RNA-binding protein influx (Glaunsinger et al., 2005; Kumar and Glaunsinger, 2010; Elliot et al., 2018).
393 Interestingly, KSHV encodes an RNA, PAN, that rescues nuclear export of viral mRNAs (Withers et al.,
394 2018). An intriguing possibility is that the PAN RNA titrates RBPs that interfere with nuclear export,
395 thereby allowing export of the herpes mRNAs. Thus, RBP re-localization can be either host- or viral-
396 mediated and can potentially alter both host and viral gene expression. Lastly, the inhibition of host-
397 mediated RNA decay by viruses, such as by flavivirus sfRNA-mediated inhibition of XRN-1 or poliovirus-
398 mediated inhibition of RNase L (Moon et al., 2012; Han et al., 2007), may regulate host RBP interactions
399 with the viral RNA. Elucidating how overall RNA abundance and subcellular location regulates the
400 availability RBPs to modulate both host and viral RNA function will be an important issue to address.
401
402 An interesting observation is that SARS-CoV-2 infection, which results in rapid degradation of
403 host mRNAs even in the absence of RNase L through the action of the SAR2 Nsp1 protein (Burke et al.,
404 2021b), does not trigger robust PABP translocation to the nucleus as demonstrated by the lack of nuclear
405 PABP staining in SARS-CoV-2 infected RL-KO cells (Fig 7B,D,E). We suggest two possibilities to explain
406 this phenomenon. First, the difference in the RNA decay mechanisms between RNase L and SARS-CoV-
407 2 Nsp1 could result in differential release of RBPs such as PABP from RNAs. Second, SARS-CoV-2 may
408 prevent RBP influx into the nucleus, and RNase L overcomes this inhibitory mechanism. Nevertheless,
409 during SARS-CoV-2 infection we still observed more IFNB1 DoG RNAs in WT cells than RL-KO cells,
410 indicating that DoG generation is a consequence of RNase L activation in response to SARS-CoV-2
411 infection. Whether this is beneficial for SARS-CoV-2 since it reduces host antiviral gene expression is
412 unclear. However, since RNase L only reduces SARS-CoV-2 replication via decay of the viral mRNA by
413 only 3-4 fold (Li et al., 2021; Burke et al., 2021), perhaps the potential loss of fitness of allowing RNase L
414 activation is outweighed by the perturbation in host interferon production.
415
416 Our data establish that RNase L activation promotes the formation of DoG transcription read-
417 through. Interestingly, while DoG transcripts are generally retained at the site of transcription (Vilborg et
418 al, 2015), we observed abundant IFNB1 DoG transcripts that contained the IFNB1 CDS disseminated

419 throughout the nucleus (Fig. 6A,B). Moreover, the IFNB1 transcripts with DoG RNA were almost
420 exclusively localized to the nucleus, whereas IFNB1 transcripts in the same cells without the DoG RNA
421 were localized to the cytoplasm. These observations suggest that the DoG RNA on IFNB1 transcripts
422 inhibits their mRNA export, even after their release from the site of transcription. The inclusion of
423 downstream elements on the IFNB1 mRNA transcript may present a new RNase L-dependent regulatory
424 mechanism, which will be a focus of future work.
425
426 While much lower in abundance and more localized to the IFNB1 transcription site in comparison
427 to WT cells, the IFNB1 DoG also formed in RL-KO cells (Fig. 5B). This indicates that IFNB1 DoG
428 formation is a normal aspect of IFNB1 gene induction. However, unlike IFNB1, we did not observe any
429 IFNL1 DoG RNA in RL-KO cells. Thus, DoG transcriptional read-through is differential with respect to
430 different dsRNA-induced genes. Understanding this difference may reveal key aspects for transcriptional
431 and RNA processing regulatory mechanisms of these genes.
432
433 The RNA processing defects promoted by RNase L activation, such as DoG read-through
434 transcription and splicing alterations (alternative splicing and intron retention), may prove to be new
435 antiviral mechanisms that perturb viral gene expression or promote the host immune response. For example,
436 DoG transcriptional read-through of dsDNA viral genomes could interfere with productive viral gene
437 expression and/or generate PAMPs that could trigger antiviral PRRs. Moreover, since RBPs can directly
438 modulate transcription (Xiao et al., 2019), this work strongly implies that widespread RNA degradation in
439 the cytosol will lead to changes in transcription of multiple genes due to the influx of RBPs into the nucleus.
440 Future work will examine these potential functions and address the specific mechanism by which RNase L
441 activation alters nuclear RNA processing and transcription.

ACKNOWLEDGMENTS

Research reported in this publication was supported by the National Institute of Allergy and Infectious Diseases of the National Institutes of Health under Award Number F32AI145112 (J.M.B), funds from HHMI (Roy Parker), National Institutes of Health R01-AI-137011 (S.L.S.), and support provided by the Office of the Vice President for Research and the Dept. of Microbiology, Immunology and Pathology at Colorado State University (Rushika Perera),

AUTHOR CONTRIBUTIONS

J.M.B. and Roy Parker conceived the project. J.M.B. performed poly(I:C) transfections, western blots, microscopy, and quantification of microscopy. N.R. performed RNA-seq analyses. M.B.F performed splicing analyses and validation. E.R.W.S. performed DENV infections. L.A.S. performed SARS-CoV-2 infections. J.M.B., N.R., and Roy Parker interpreted the data. J.M.B., N.R., and Roy Parker wrote the manuscript.

CONFLICT OF INTEREST

Roy Parker is a founder and consultant of Faze Medicines. The authors declare that they have no other competing interests.

459 **MATERIALS & METHODS**

460

461 *Cell culture*

462 Parental and RNase L knockout A549 cell lines are described in Burke et al., 2019. Cells were
463 maintained at 5% CO_2 and 37 degrees Celsius in Dulbecco's modified eagle' medium (DMEM)
464 supplemented with fetal bovine serum (FBS; 10% v/v) and penicillin/streptomycin (1% v/v). Routine
465 testing for mycoplasma contamination was performed by the cell culture core facility. African green
466 monkey kidney cells (Vero E6, ATCC CRL-1586) were maintained at 5% CO_2 and 37 degrees Celsius in
467 DMEM supplemented with FBS (10% v/v), 2 mM non-essential amino acids, 2 mM l-glutamine, and 25
468 mM HEPES buffer.

469

470 For transfections, high-molecular weight poly(I:C) (InvivoGen: tlrl-pic) and 3-µl of lipofectamine
471 2000 (Thermo Fisher Scientific) per 1-ug or poly(I:C) was used per manufacturer's instructions.

472

473 *Viral infections*

474 Viral infections are described in Burke et al., 2021a and Burke et al., 2021b. Briefly, cells were
475 infected with DENV serotype 2 16681 strain at MOI of 1.0. Cells were fixed 48 hours after infection.
476 SARS-CoV-2/WA/20/01 (GenBank MT020880; BEI Resources: NR-52881) was passaged in Vero E6
477 cells, and viral titer was determined via plaque assay on Vero E6 as previously described in (Dulbecco et
478 al., 1953). A multiplicity of infection (MOI) of 5 was used. All SARS-CoV-2 infections were conducted
479 under biosafety level 3 conditions at Colorado State University. Dengue virus infections were conducted
480 under biosafety level 3 conditions at University of Colorado, Boulder. For infections, cells were seeded in
481 6-wells format onto cover slips and inoculated twenty-four hours later. Cells were fixed in 4%
482 paraformaldehyde and phosphate-buffered saline (PBS) for 20 minutes, followed by three five-minute
483 washes with 1X PBS, and stored in 75% ethanol.

484

485 *RNA-seq analysis*

486 Our previously published RNA-seq data (Burke et al., 2019) were re-processed using a Nextflow
487 pipeline (https://github.com/Dowell-Lab/RNAseq-Flow). Normalized TDF files that were generated by the
488 pipeline were used to visualize representative gene traces with the Integrative Genomics Viewer (Robinson
489 et al., 2012). Exon or intron reads were counted for each sorted BAM file over annotated genes in the
490 RefSeq hg38 genome using featureCounts (Rsubread/2.0.1,(Liao et al., 2013). GTFtools was used to
491 determine intron boundaries (Hong-Dong Li e al., 2018) and to generate an introns only gtf file. RNA
492 isoforms were filtered for the highest expressed isoform equivalent to the highest FPKM value in the WT

493 condition. DESeq2/1.26.0 was used for differential expression analysis. ERCC RNA Spike-Ins were used
494 to estimate and correct size factors in DESeq2. In particular, ERCC Spike-Ins reads were mapped using the
495 same Nextflow pipeline to the ERCC sequences
496 (https://tools.thermofisher.com/content/sfs/manuals/ERCC92.zip), counted using featureCounts and the
497 ERCC Spike-Ins size factors derived by DESeq2. Significant differentially upregulated or downregulated
498 RNAs were selected by baseMean >5, padj < 0.05 and a log2fold change of 1. Nonsignificant genes were
499 selected by padj > 0.05 and log2fold change of -0.5 to 0.5.
500 Intron retention analysis was performed on all RNAs with the Deseq2 baseMean cutoff > 30, to
501 remove RNAs with too low counts. Intron/exon ratios were derived by diving the TPM normalized intron
502 counts by TPM normalized exon counts. Intron/exon ratios > 8.5 were a result from "towers" in intronic
503 regions, counts in non-annotated regions, noise due to low counts or read-through from an upstream gene.
504 Therefore, all intron/exon ratios >8.5 were removed from analysis.
505 DoG formation was estimated similarly, by generating TPM normalized counts over the first 5000
506 pb following the exon annotation. These TPM normalized $DoG_{1\text{-}5000}$ counts were divided by the TPM
507 normalized exon counts to derive and a DoG/exon ratio. For the same reasons as describe for intron/exon
508 ratios, DoG/exon ratios > 5 were removed from analysis. Moreover, small RNAs (exon size < 300bp) were
509 removed from analysis.
510 In our ratio analysis, genes were not filtered for "clean" genes, genes that have counts due to
511 expression and not due to read-through transcription from up-coming gene (Rosa-Mercado et al., 2021).
512 However, many genes that were not expression but showed read-through transcription from up-coming
513 gene were filtered out by the intron/exon ratios >15 and DoG/exon ratios > 5 step. We do anticipate false-
514 positives left in our analysis, especially in the upregulated group.
515 Figures were made using ggplot2/3.3.3.
516 For the splicing analysis, raw fastq reads were trimmed to remove adapters and low quality reads
517 with bbduk/38.79 (Bushnell, 2014), aligned to the hg38 genome using STAR/2.5.2a (Dobin et al., 2013),
518 sorted and indexed with samtools/1.9 (Li et al., 2009), and then analyzed with MAJIQ/2.0 (Vaquero-Garcia
519 et al., 2016). Splicing events were quantified for downstream analysis using the voila classify function,
520 which groups splicing events into distinct modules. Events were considered significant if the probability of
521 having a ΔPSI > 10 was greater than 90%.
522
523 *RT-PCR analysis of splicing*
524 Validation of splicing events by low-cycle radiolabeled PCR was performed as previously described (Lynch
525 and Weiss, 2000) with the following modifications. Annealing temperatures during PCR amplification, and
526 the number of cycles required to maintain the signal in the linear range, were determined empirically for

527 each splicing event. Gene specific primers are listed in Table S1 and were designed with the aid of MAJIQ's
528 voila visualization tool.
529
530 *Immunoblot analyses*
531 Immunoblot analysis was performed as described in Burke et al., 2019. Rabbit anti-GAPDH (Cell
532 Signaling Technology: 2118L) was used at 1:2000. Anti-rabbit immunoglobulin G (IgG), horseradish
533 peroxidase (HRP)–linked antibody (Cell Signaling Technology: 7074S) was used at 1:3000. Anti-mouse
534 IgG, HRP-linked antibody (Cell Signaling Technology: 7076S) was used at 1:10,000. Histone H3 antibody
535 (Thermo Fisher Scientific; NB500-171) was used at 1:1000. Crude nuclear and cytoplasmic fractionation
536 was performed as described in Burke et al., 2017.
537
538 *Immunofluorescence and smFISH*
539 smFISH was performed as described in Burke et al., 2019 and following the manufacturer's
540 protocol
541 (https://biosearchassets.blob.core.windows.net/assets/bti_custom_stellaris_immunofluorescence_seq_prot
542 ocol.pdf). GAPDH smFISH probes labeled with Quasar 570 dye (SMF-2026-1) were purchased from
543 Stellaris. Custom IFNB1, IFNL1, SARS-CoV-2, and DENV2 smFISH probes were designed using Stellaris
544 smFISH probe designer (Biosearch Technologies) available online at http://biosearchtech.com/stellaris-
545 designer. Reverse complement DNA oligos were purchased from IDT (Data file S1). The probes were
546 labeled with ATTO-633 using ddUTP-Atto633 (Axxora: JBS-NU-1619-633), ATTO-550 using 5-
547 Propargylamino-ddUTP (Axxora; JBS-NU-1619-550), or ATTO-488 using 5-Propargylamino-ddUTP
548 (Axxora; JBS-NU-1619-488) with terminal deoxynucleotidyl transferase (Thermo Fisher Scientific:
549 EP0161) as described in Gaspar et al., 2017.
550
551 *Microscopy and image analysis*
552 Coverslips were mounted on slides with VECTASHIELD Antifade Mounting Medium containing
553 4′,6-diamidino-2-phenylindole (DAPI) (Vector Laboratories; H-1200). Images were obtained using a wide-
554 field DeltaVision Elite microscope with a 100× objective using a PCO Edge sCMOS camera. Between 10
555 and 15 Z planes at 0.2 µm per section were taken for each image. Deconvoluted images were processed
556 using ImageJ with FIJI plugin. Z planes were stacked, and minimum and maximum display values were set
557 in ImageJ for each channel to properly view fluorescence. Fluorescence intensity was measured in ImageJ.
558 Single cells were outlined by determining the cell boundaries via background fluorescence and mean
559 intensity was measured in the relevant channels. Imaris Image Analysis Software (Bitplane) (University of
560 Colorado Boulder, BioFrontiers Advanced Light Microscopy Core) was used to quantify smFISH foci in

561 nucleus and cytoplasm. Single cells were isolated for analysis by defining their borders via background
562 fluorescence. Total foci above background threshold intensity were counted. Afterward, the nucleus marked
563 with DAPI was masked, and foci were counted in the cell at the same intensity threshold cutoff, yielding
564 the cytoplasmic foci count, from which the nuclear foci number could be determined.
565
566 *Figure generation*
567 The model figure was created with BioRender.com.

568 **REFERENCES**

569 Al-Ahmadi W, Al-Haj L, Al-Mohanna FA, Silverman RH, Khabar KS. RNase L downmodulation of the
570 RNA-binding protein, HuR, and cellular growth. Oncogene. 2009 Apr 16;28(15):1782-91. doi:
571 10.1038/onc.2009.16. Epub 2009 Mar 2. PMID: 19252527; PMCID: PMC3071643.
572 Andersen JB, Mazan-Mamczarz K, Zhan M, Gorospe M, Hassel BA. Ribosomal protein mRNAs are
573 primary targets of regulation in RNase-L-induced senescence. RNA Biol. 2009 Jul-Aug;6(3):305-
574 15. doi: 10.4161/rna.6.3.8526. Epub 2009 Jul 23. PMID: 19411840; PMCID: PMC2752476.
575 Bauer DLV, Tellier M, Martínez-Alonso M, Nojima T, Proudfoot NJ, Murphy S, Fodor E. Influenza
576 Virus Mounts a Two-Pronged Attack on Host RNA Polymerase II Transcription. Cell Rep. 2018
577 May 15;23(7):2119-2129.e3. doi: 10.1016/j.celrep.2018.04.047. PMID: 29768209; PMCID:
578 PMC5972227.
579 Bayard BA, Gabrion JB. 2',5'-Oligoadenylate-dependent RNAse located in nuclei: biochemical
580 characterization and subcellular distribution of the nuclease in human and murine cells. Biochem
581 J. 1993 Nov 15;296 (Pt 1)(Pt 1):155-60. doi: 10.1042/bj2960155. PMID: 8250837; PMCID:
582 PMC1137668.
583 Burke JM, Gilchrist AR, Sawyer SL, Parker R. RNase L limits host and viral protein synthesis via
584 inhibition of mRNA export. Sci Adv. 2021 Jun 4;7(23):eabh2479. doi: 10.1126/sciadv.abh2479.
585 PMID: 34088676; PMCID: PMC8177694.
586 Burke JM, Lester ET, Tauber D, Parker R. RNase L promotes the formation of unique ribonucleoprotein
587 granules distinct from stress granules. J Biol Chem. 2020 Feb 7;295(6):1426-1438. doi:
588 10.1074/jbc.RA119.011638. Epub 2020 Jan 2. PMID: 31896577; PMCID: PMC7008361.
589 Burke JM, Moon SL, Matheny T, Parker R. RNase L Reprograms Translation by Widespread mRNA
590 Turnover Escaped by Antiviral mRNAs. Mol Cell. 2019 Sep 19;75(6):1203-1217.e5. doi:
591 10.1016/j.molcel.2019.07.029. Epub 2019 Sep 4. PMID: 31494035; PMCID: PMC6754297.
592 Burke JM, St Clair LA, Perera R, Parker R. SARS-CoV-2 infection triggers widespread host mRNA
593 decay leading to an mRNA export block. RNA. 2021 Nov;27(11):1318-1329. doi:
594 10.1261/rna.078923.121. Epub 2021 Jul 27. PMID: 34315815; PMCID: PMC8522697.
595 Burke JM, Sullivan CS. DUSP11 - An RNA phosphatase that regulates host and viral non-coding RNAs
596 in mammalian cells. RNA Biol. 2017 Nov 2;14(11):1457-1465. doi:
597 10.1080/15476286.2017.1306169. Epub 2017 Apr 17. PMID: 28296624; PMCID: PMC5785229.
598 Bushnell B. BBMap: A Fast, Accurate, Splice-Aware Aligner. N.p. (2014), (available at
599 https://sourceforge.net/projects/bbmap/).
600 Cáceres JF, Screaton GR, Krainer AR. A specific subset of SR proteins shuttles continuously between the
601 nucleus and the cytoplasm. Genes Dev. 1998 Jan 1;12(1):55-66. doi: 10.1101/gad.12.1.55. PMID:
602 9420331; PMCID: PMC316398.
603 Carolyn J. Decker, James M. Burke, Patrick K. Mulvaney, Roy Parker. RNA is required for the
604 maintenance of multiple cytoplasmic and nuclear membrane-less organelles. bioRxiv
605 2021.08.16.456519; doi: https://doi.org/10.1101/2021.08.16.456519
606 Cooper DA, Banerjee S, Chakrabarti A, García-Sastre A, Hesselberth JR, Silverman RH, Barton DJ.
607 RNase L targets distinct sites in influenza A virus RNAs. J Virol. 2015 Mar;89(5):2764-76. doi:
608 10.1128/JVI.02953-14. Epub 2014 Dec 24. PMID: 25540362; PMCID: PMC4325751.
609 Dobin A, Davis CA, Schlesinger F, Drenkow J, Zaleski C, Jha S, Batut P, Chaisson M, Gingeras TR.
610 STAR: ultrafast universal RNA-seq aligner. Bioinformatics. 2013 Jan 1;29(1):15-21. doi:
611 10.1093/bioinformatics/bts635. Epub 2012 Oct 25. PMID: 23104886; PMCID: PMC3530905.
612 Donovan J, Rath S, Kolet-Mandrikov D, Korennykh A. Rapid RNase L-driven arrest of protein synthesis
613 in the dsRNA response without degradation of translation machinery. RNA. 2017
614 Nov;23(11):1660-1671. doi: 10.1261/rna.062000.117. Epub 2017 Aug 14. PMID: 28808124;
615 PMCID: PMC5648034.
616 Dulbecco R, Vogt M. Some problems of animal virology as studied by the plaque technique. Cold Spring
617 Harb Symp Quant Biol. 1953;18:273-9. doi: 10.1101/sqb.1953.018.01.039. PMID: 13168995.

618 Elliott G, Pheasant K, Ebert-Keel K, Stylianou J, Franklyn A, Jones J. Multiple Posttranscriptional
619 Strategies To Regulate the Herpes Simplex Virus 1 vhs Endoribonuclease. J Virol. 2018 Aug
620 16;92(17):e00818-18. doi: 10.1128/JVI.00818-18. PMID: 29925667; PMCID: PMC6096803.
621 Floyd-Smith G, Slattery E, Lengyel P. Interferon action: RNA cleavage pattern of a (2'-5')oligoadenylate-
622 -dependent endonuclease. Science. 1981 May 29;212(4498):1030-2. doi:
623 10.1126/science.6165080. PMID: 6165080.
624 Gaspar I, Wippich F, Ephrussi A. Enzymatic production of single-molecule FISH and RNA capture
625 probes. RNA. 2017 Oct;23(10):1582-1591. doi: 10.1261/rna.061184.117. Epub 2017 Jul 11.
626 PMID: 28698239; PMCID: PMC5602115.
627 Gilbertson S, Federspiel JD, Hartenian E, Cristea IM, Glaunsinger B. Changes in mRNA abundance drive
628 shuttling of RNA binding proteins, linking cytoplasmic RNA degradation to transcription. Elife.
629 2018 Oct 3;7:e37663. doi: 10.7554/eLife.37663. PMID: 30281021; PMCID: PMC6203436.
630 Glaunsinger B, Chavez L, Ganem D. The exonuclease and host shutoff functions of the SOX protein of
631 Kaposi's sarcoma-associated herpesvirus are genetically separable. J Virol. 2005
632 Jun;79(12):7396-401. doi: 10.1128/JVI.79.12.7396-7401.2005. PMID: 15919895; PMCID:
633 PMC1143623.
634 Han JQ, Townsend HL, Jha BK, Paranjape JM, Silverman RH, Barton DJ. A phylogenetically conserved
635 RNA structure in the poliovirus open reading frame inhibits the antiviral endoribonuclease RNase
636 L. J Virol. 2007 Jun;81(11):5561-72. doi: 10.1128/JVI.01857-06. Epub 2007 Mar 7. PMID:
637 17344297; PMCID: PMC1900262.
638 Hong-Dong Li. GTFtools: a Python package for analyzing various modes of gene models. bioRxiv
639 263517; doi: https://doi.org/10.1101/263517.
640 Kedersha NL, Gupta M, Li W, Miller I, Anderson P. RNA-binding proteins TIA-1 and TIAR link the
641 phosphorylation of eIF-2 alpha to the assembly of mammalian stress granules. J Cell Biol. 1999
642 Dec 27;147(7):1431-42. doi: 10.1083/jcb.147.7.1431. PMID: 10613902; PMCID: PMC2174242.
643 Khong A, Matheny T, Jain S, Mitchell SF, Wheeler JR, Parker R. The Stress Granule Transcriptome
644 Reveals Principles of mRNA Accumulation in Stress Granules. Mol Cell. 2017 Nov
645 16;68(4):808-820.e5. doi: 10.1016/j.molcel.2017.10.015. Epub 2017 Nov 9. PMID: 29129640;
646 PMCID: PMC5728175.
647 Kristiansen H, Gad HH, Eskildsen-Larsen S, Despres P, Hartmann R. The oligoadenylate synthetase
648 family: an ancient protein family with multiple antiviral activities. J Interferon Cytokine Res.
649 2011 Jan;31(1):41-7. doi: 10.1089/jir.2010.0107. Epub 2010 Dec 12. PMID: 21142819.
650 Kumar GR, Glaunsinger BA. Nuclear import of cytoplasmic poly(A) binding protein restricts gene
651 expression via hyperadenylation and nuclear retention of mRNA. Mol Cell Biol. 2010
652 Nov;30(21):4996-5008. doi: 10.1128/MCB.00600-10. Epub 2010 Sep 7. PMID: 20823266;
653 PMCID: PMC2953054.
654 Liao Y, Smyth GK, Shi W. The Subread aligner: fast, accurate and scalable read mapping by seed-and-
655 vote. Nucleic Acids Res. 2013 May 1;41(10):e108. doi: 10.1093/nar/gkt214. Epub 2013 Apr 4.
656 PMID: 23558742; PMCID: PMC3664803.
657 Li H, Handsaker B, Wysoker A, Fennell T, Ruan J, Homer N, Marth G, Abecasis G, Durbin R; 1000
658 Genome Project Data Processing Subgroup. The Sequence Alignment/Map format and
659 SAMtools. Bioinformatics. 2009 Aug 15;25(16):2078-9. doi: 10.1093/bioinformatics/btp352.
660 Epub 2009 Jun 8. PMID: 19505943; PMCID: PMC2723002.
661 Li Y, Banerjee S, Wang Y, Goldstein SA, Dong B, Gaughan C, Silverman RH, Weiss SR. Activation of
662 RNase L is dependent on OAS3 expression during infection with diverse human viruses. Proc
663 Natl Acad Sci U S A. 2016 Feb 23;113(8):2241-6. doi: 10.1073/pnas.1519657113. Epub 2016
664 Feb 8. Erratum in: Proc Natl Acad Sci U S A. 2019 Jun 18;116(25):12573. PMID: 26858407;
665 PMCID: PMC4776461.
666 Li Y, Renner DM, Comar CE, Whelan JN, Reyes HM, Cardenas-Diaz FL, Truitt R, Tan LH, Dong B,
667 Alysandratos KD, Huang J, Palmer JN, Adappa ND, Kohanski MA, Kotton DN, Silverman RH,
668 Yang W, Morrisey EE, Cohen NA, Weiss SR. SARS-CoV-2 induces double-stranded RNA-

669 mediated innate immune responses in respiratory epithelial-derived cells and cardiomyocytes.
670 Proc Natl Acad Sci U S A. 2021 Apr 20;118(16):e2022643118. doi: 10.1073/pnas.2022643118.
671 PMID: 33811184; PMCID: PMC8072330.
672 Li Z, Nagy PD. Diverse roles of host RNA binding proteins in RNA virus replication. RNA Biol. 2011
673 Mar-Apr;8(2):305-15. doi: 10.4161/rna.8.2.15391. Epub 2011 Mar 1. PMID: 21505273; PMCID:
674 PMC3230553.
675 Lynch KW, Weiss A. A model system for activation-induced alternative splicing of CD45 pre-mRNA in
676 T cells implicates protein kinase C and Ras. Mol Cell Biol. 2000 Jan;20(1):70-80. doi:
677 10.1128/MCB.20.1.70-80.2000. PMID: 10594010; PMCID: PMC85051.
678 Min JY, Krug RM. The primary function of RNA binding by the influenza A virus NS1 protein in
679 infected cells: Inhibiting the 2'-5' oligo (A) synthetase/RNase L pathway. Proc Natl Acad Sci U S
680 A. 2006 May 2;103(18):7100-5. doi: 10.1073/pnas.0602184103. Epub 2006 Apr 20. PMID:
681 16627618; PMCID: PMC1459024.
682 Moon SL, Anderson JR, Kumagai Y, Wilusz CJ, Akira S, Khromykh AA, Wilusz J. A noncoding RNA
683 produced by arthropod-borne flaviviruses inhibits the cellular exoribonuclease XRN1 and alters
684 host mRNA stability. RNA. 2012 Nov;18(11):2029-40. doi: 10.1261/rna.034330.112. Epub 2012
685 Sep 24. PMID: 23006624; PMCID: PMC3479393.
686 Müller-McNicoll M, Rossbach O, Hui J, Medenbach J. Auto-regulatory feedback by RNA-binding
687 proteins. J Mol Cell Biol. 2019 Oct 25;11(10):930-939. doi: 10.1093/jmcb/mjz043. PMID:
688 31152582; PMCID: PMC6884704.
689 Nogimori T, Nishiura K, Kawashima S, Nagai T, Oishi Y, Hosoda N, Imataka H, Kitamura Y, Kitade Y,
690 Hoshino SI. Dom34 mediates targeting of exogenous RNA in the antiviral OAS/RNase L
691 pathway. Nucleic Acids Res. 2019 Jan 10;47(1):432-449. doi: 10.1093/nar/gky1087. PMID:
692 30395302; PMCID: PMC6326797.
693 Onomoto K, Jogi M, Yoo JS, Narita R, Morimoto S, Takemura A, Sambhara S, Kawaguchi A, Osari S,
694 Nagata K, Matsumiya T, Namiki H, Yoneyama M, Fujita T. Critical role of an antiviral stress
695 granule containing RIG-I and PKR in viral detection and innate immunity. PLoS One.
696 2012;7(8):e43031. doi: 10.1371/journal.pone.0043031. Epub 2012 Aug 13. Erratum in: PLoS
697 One. 2012;7(10). doi:10.1371/annotation/dcd836ee-9e23-4538-acb7-450560ba5c1d. Erratum in:
698 PLoS One. 2013;8(4). doi:10.1371/annotation/14a6b875-ed9d-41ae-8ce6-52e8c5c7f85b. PMID:
699 22912779; PMCID: PMC3418241.
700 Rath S, Prangley E, Donovan J, Demarest K, Wingreen NS, Meir Y, Korennykh A. Concerted 2-5A-
701 Mediated mRNA Decay and Transcription Reprogram Protein Synthesis in the dsRNA Response.
702 Mol Cell. 2019 Sep 19;75(6):1218-1228.e6. doi: 10.1016/j.molcel.2019.07.027. Epub 2019 Sep
703 4. PMID: 31494033; PMCID: PMC6754276.
704 Reineke LC, Lloyd RE. The stress granule protein G3BP1 recruits protein kinase R to promote multiple
705 innate immune antiviral responses. J Virol. 2015 Mar;89(5):2575-89. doi: 10.1128/JVI.02791-14.
706 Epub 2014 Dec 17. PMID: 25520508; PMCID: PMC4325707.
707 Robinson JT, Thorvaldsdóttir H, Winckler W, Guttman M, Lander ES, Getz G, Mesirov JP. Integrative
708 genomics viewer. Nat Biotechnol. 2011 Jan;29(1):24-6. doi: 10.1038/nbt.1754. PMID: 21221095;
709 PMCID: PMC3346182.
710 Rosa-Mercado NA, Zimmer JT, Apostolidi M, Rinehart J, Simon MD, Steitz JA. Hyperosmotic stress
711 alters the RNA polymerase II interactome and induces readthrough transcription despite
712 widespread transcriptional repression. Mol Cell. 2021 Feb 4;81(3):502-513.e4. doi:
713 10.1016/j.molcel.2020.12.002. Epub 2021 Jan 4. PMID: 33400923; PMCID: PMC7867636.
714 Rutkowski AJ, Erhard F, L'Hernault A, Bonfert T, Schilhabel M, Crump C, Rosenstiel P, Efstathiou S,
715 Zimmer R, Friedel CC, Dölken L. Widespread disruption of host transcription termination in
716 HSV-1 infection. Nat Commun. 2015 May 20;6:7126. doi: 10.1038/ncomms8126. PMID:
717 25989971; PMCID: PMC4441252.

718 Silverman RH. Viral encounters with 2',5'-oligoadenylate synthetase and RNase L during the interferon
719 antiviral response. J Virol. 2007 Dec;81(23):12720-9. doi: 10.1128/JVI.01471-07. Epub 2007 Sep
720 5. PMID: 17804500; PMCID: PMC2169107.
721 Vaquero-Garcia J, Barrera A, Gazzara MR, González-Vallinas J, Lahens NF, Hogenesch JB, Lynch KW,
722 Barash Y. A new view of transcriptome complexity and regulation through the lens of local
723 splicing variations. Elife. 2016 Feb 1;5:e11752. doi: 10.7554/eLife.11752. PMID: 26829591;
724 PMCID: PMC4801060.
725 Vilborg A, Passarelli MC, Yario TA, Tycowski KT, Steitz JA. Widespread Inducible Transcription
726 Downstream of Human Genes. Mol Cell. 2015 Aug 6;59(3):449-61. doi:
727 10.1016/j.molcel.2015.06.016. Epub 2015 Jul 16. PMID: 26190259; PMCID: PMC4530028.
728 Vilborg A, Steitz JA. Readthrough transcription: How are DoGs made and what do they do? RNA Biol.
729 2017 May 4;14(5):632-636. doi: 10.1080/15476286.2016.1149680. Epub 2016 Feb 9. PMID:
730 26861889; PMCID: PMC5449079.
731 Withers JB, Li ES, Vallery TK, Yario TA, Steitz JA. Two herpesviral noncoding PAN RNAs are
732 functionally homologous but do not associate with common chromatin loci. PLoS Pathog. 2018
733 Nov 1;14(11):e1007389. doi: 10.1371/journal.ppat.1007389. PMID: 30383841; PMCID:
734 PMC6233925.
735 Wreschner DH, McCauley JW, Skehel JJ, Kerr IM. Interferon action--sequence specificity of the
736 ppp(A2'p)nA-dependent ribonuclease. Nature. 1981 Jan 29;289(5796):414-7. doi:
737 10.1038/289414a0. PMID: 6162102.\
738 Xiao R, Chen JY, Liang Z, Luo D, Chen G, Lu ZJ, Chen Y, Zhou B, Li H, Du X, Yang Y, San M, Wei X,
739 Liu W, Lécuyer E, Graveley BR, Yeo GW, Burge CB, Zhang MQ, Zhou Y, Fu XD. Pervasive
740 Chromatin-RNA Binding Protein Interactions Enable RNA-Based Regulation of Transcription.
741 Cell. 2019 Jun 27;178(1):107-121.e18. doi: 10.1016/j.cell.2019.06.001. PMID: 31251911;
742 PMCID: PMC6760001.
743 Yoo JS, Takahasi K, Ng CS, Ouda R, Onomoto K, Yoneyama M, Lai JC, Lattmann S, Nagamine Y,
744 Matsui T, Iwabuchi K, Kato H, Fujita T. DHX36 enhances RIG-I signaling by facilitating PKR-
745 mediated antiviral stress granule formation. PLoS Pathog. 2014 Mar 20;10(3):e1004012. doi:
746 10.1371/journal.ppat.1004012. PMID: 24651521; PMCID: PMC3961341.
747

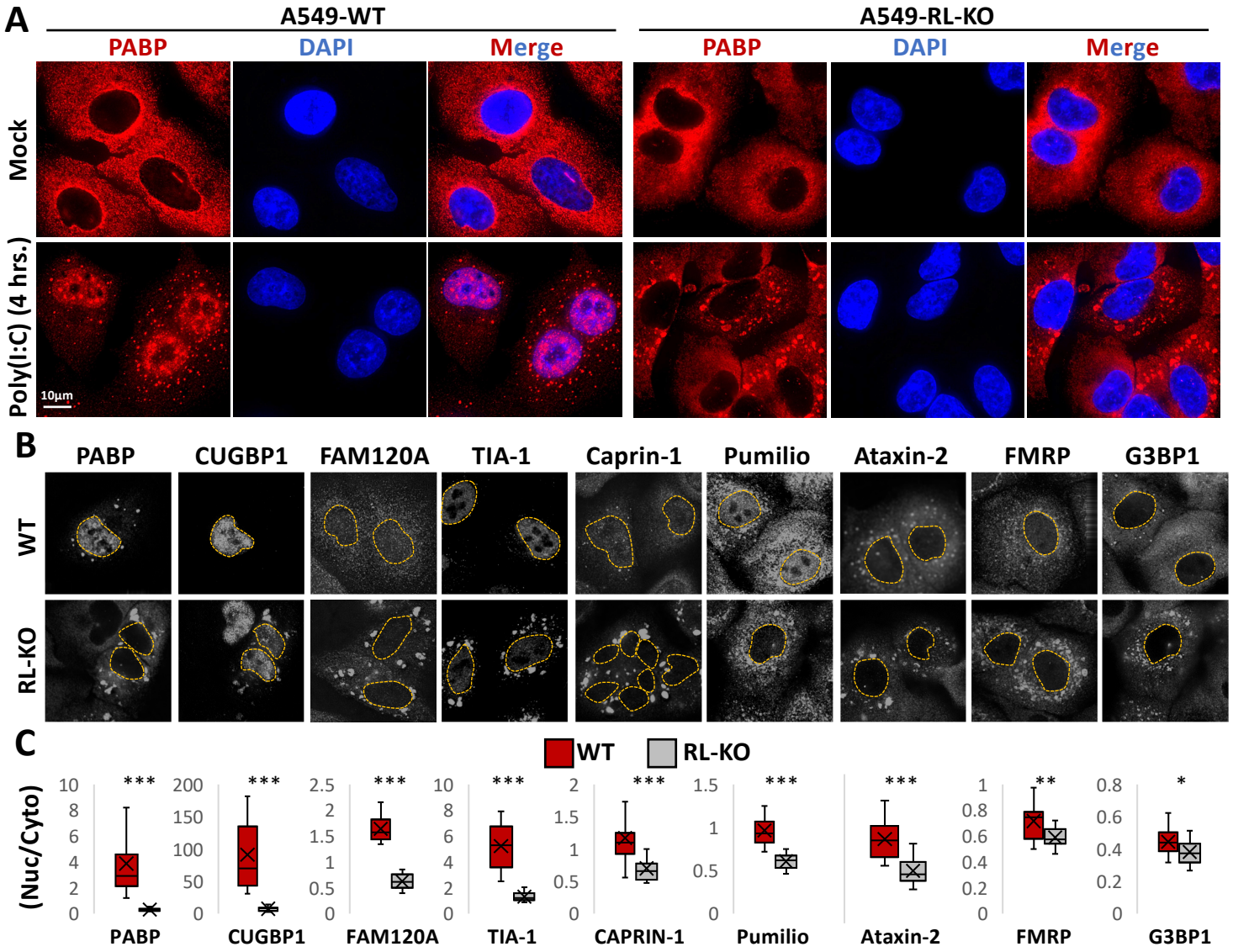
A
A549-WT
A549-RL-KO
PABP
DAPI
Merge
Mock
Poly(I:C) (4 hrs.)
10µm
B
PABP
CUGBP1
FAM120A
TIA-1
Caprin-1
Pumilio
Ataxin-2
FMRP
G3BP1
WT
RL-KO
C
WT
RL-KO
(Nuc/Cyto)
PABP
CUGBP1
FAM120A
TIA-1
CAPRIN-1
Pumilio
Ataxin-2
FMRP
G3BP1

Figure 1

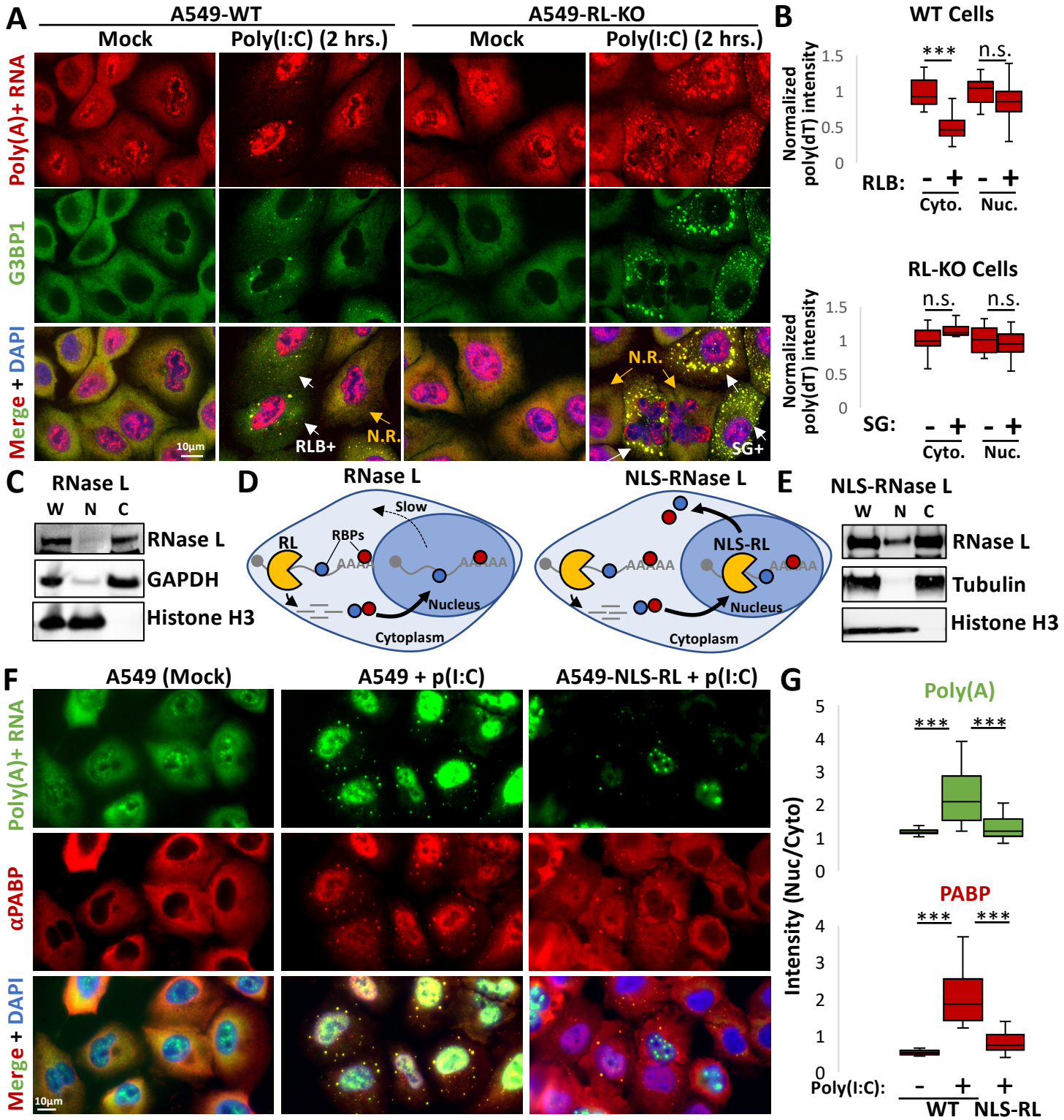
A
A549-WT
A549-RL-KO
Mock
Poly(I:C) (2 hrs.)
Mock
Poly(I:C) (2 hrs.)
Poly(A)+ RNA
G3BP1
Merge + DAPI
10µm
RLB+
N.R.
N.R.
SG+
B
WT Cells
Normalized poly(dT) intensity
1.5
1
0.5
0
***
n.s.
RLB:
-
+
-
+
Cyto.
Nuc.
RL-KO Cells
Normalized poly(dT) intensity
1.5
1
0.5
0
n.s.
n.s.
SG:
-
+
-
+
Cyto.
Nuc.
C
RNase L
W
N
C
RNase L
GAPDH
Histone H3
D
RNase L
Slow
RL
RBPs
AAAAA
AAAAA
Nucleus
Cytoplasm
NLS-RNase L
NLS-RL
AAAAA
AAAAA
Nucleus
Cytoplasm
E
NLS-RNase L
W
N
C
RNase L
Tubulin
Histone H3
F
A549 (Mock)
A549 + p(I:C)
A549-NLS-RL + p(I:C)
Poly(A)+ RNA
αPABP
Merge + DAPI
10µm
G
Poly(A)
Intensity (Nuc/Cyto)
5
4
3
2
1
0
***
***
PABP
4
3
2
1
0
***
***
Poly(I:C):
-
+
+
WT
NLS-RL

Figure 2

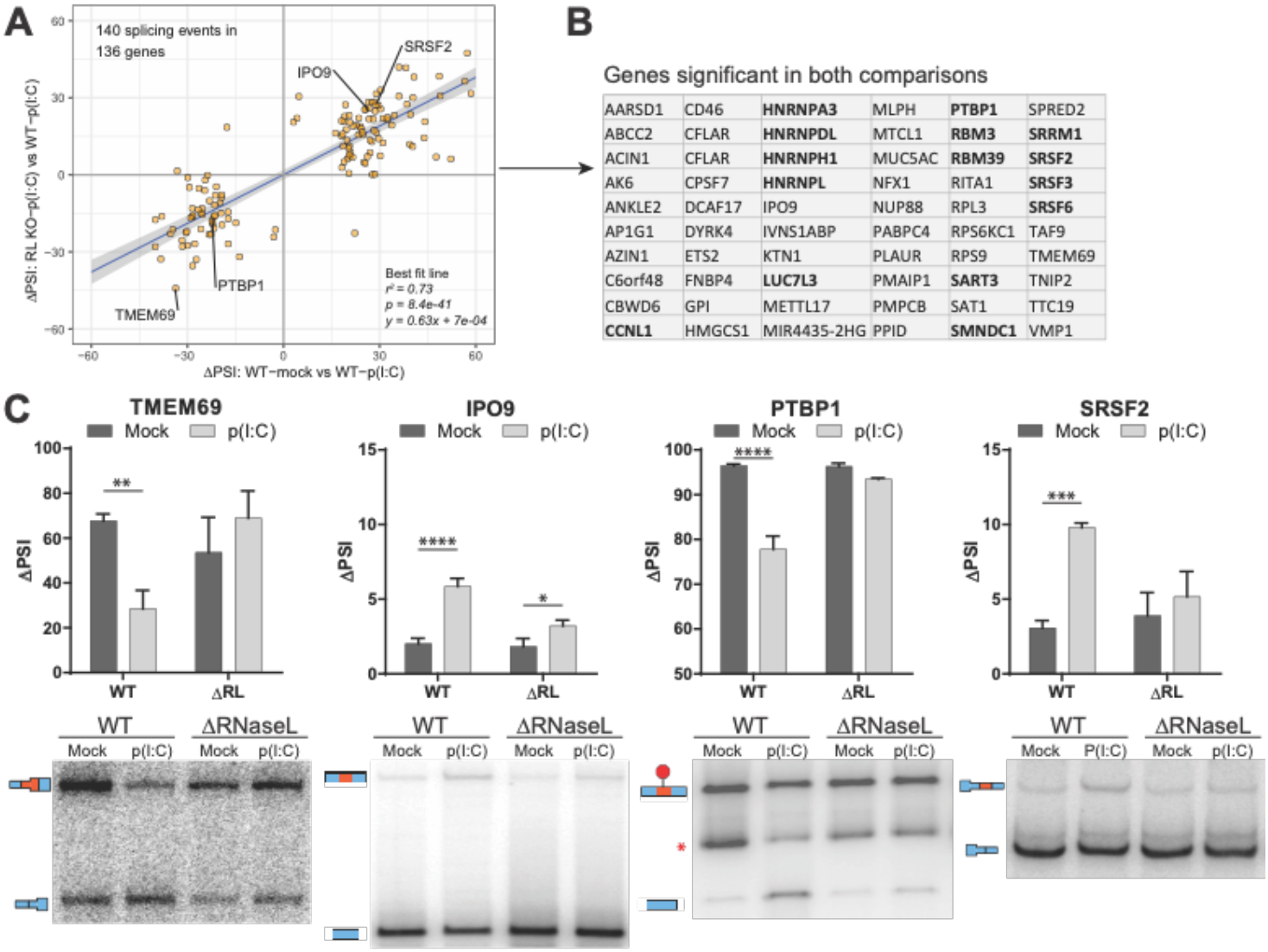

AARSD1	CD46	**HNRNPA3**	MLPH	**PTBP1**	SPRED2
ABCC2	CFLAR	**HNRNPDL**	MTCL1	**RBM3**	**SRRM1**
ACIN1	CFLAR	**HNRNPH1**	MUC5AC	**RBM39**	**SRSF2**
AK6	CPSF7	**HNRNPL**	NFX1	RITA1	**SRSF3**
ANKLE2	DCAF17	IPO9	NUP88	RPL3	**SRSF6**
AP1G1	DYRK4	IVNS1ABP	PABPC4	RPS6KC1	TAF9
AZIN1	ETS2	KTN1	PLAUR	RPS9	TMEM69
C6orf48	FNBP4	**LUC7L3**	PMAIP1	**SART3**	TNIP2
CBWD6	GPI	METTL17	PMPCB	SAT1	TTC19
CCNL1	HMGCS1	MIR4435-2HG	PPID	**SMNDC1**	VMP1

Figure 3

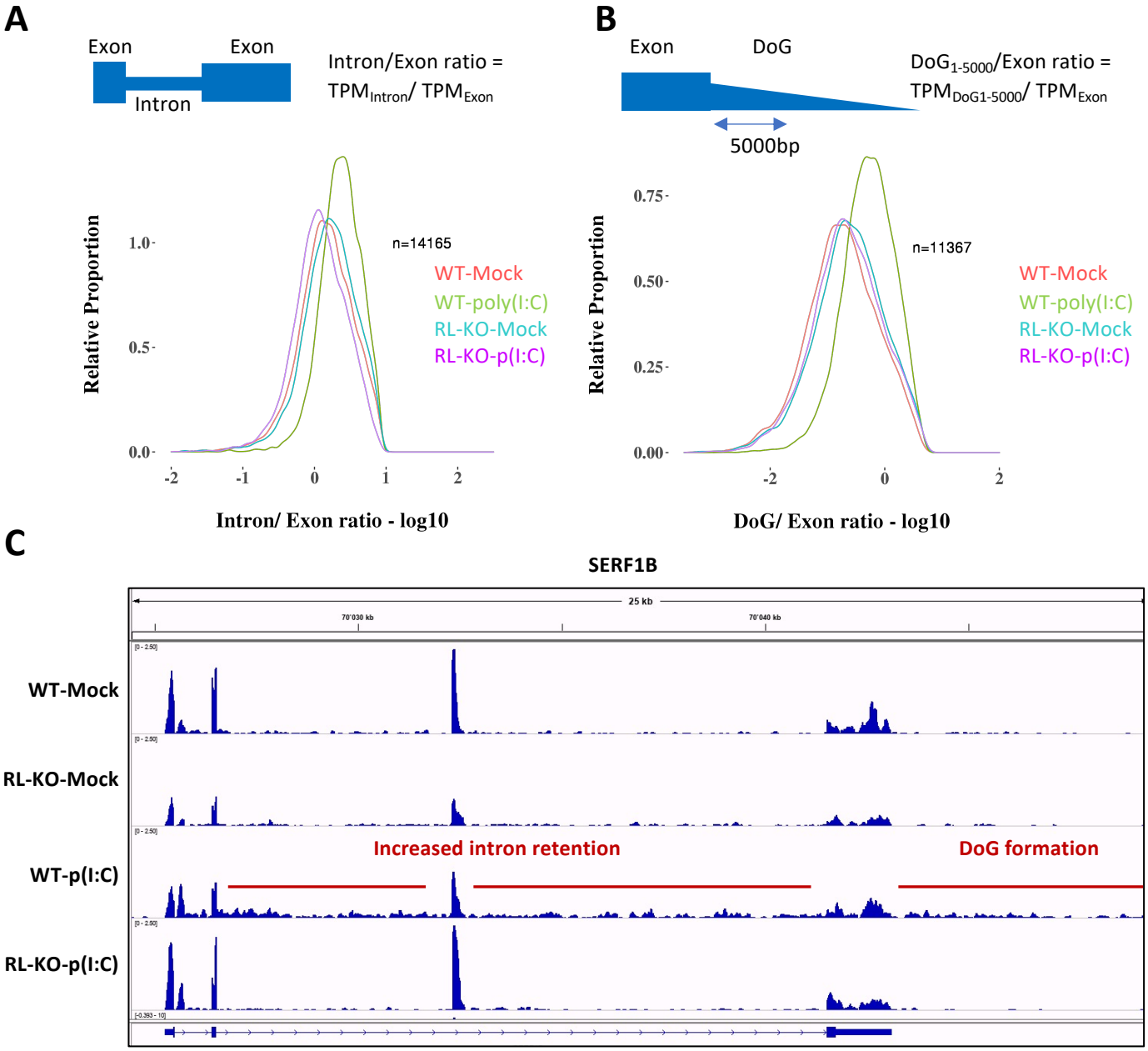
A
Exon
Exon
Intron
Intron/Exon ratio =
TPM$_{Intron}$/ TPM$_{Exon}$
Relative Proportion
1.0
0.5
0.0
-2
-1
0
1
2
n=14165
WT-Mock
WT-poly(I:C)
RL-KO-Mock
RL-KO-p(I:C)
Intron/ Exon ratio - log10
B
Exon
DoG
DoG$_{1-5000}$/Exon ratio =
TPM$_{DoG1-5000}$/ TPM$_{Exon}$
5000bp
Relative Proportion
0.75
0.50
0.25
0.00
-2
0
2
n=11367
WT-Mock
WT-poly(I:C)
RL-KO-Mock
RL-KO-p(I:C)
DoG/ Exon ratio - log10
C
SERF1B
25 kb
70'030 kb
70'040 kb
WT-Mock
RL-KO-Mock
WT-p(I:C)
RL-KO-p(I:C)
Increased intron retention
DoG formation

Figure 4

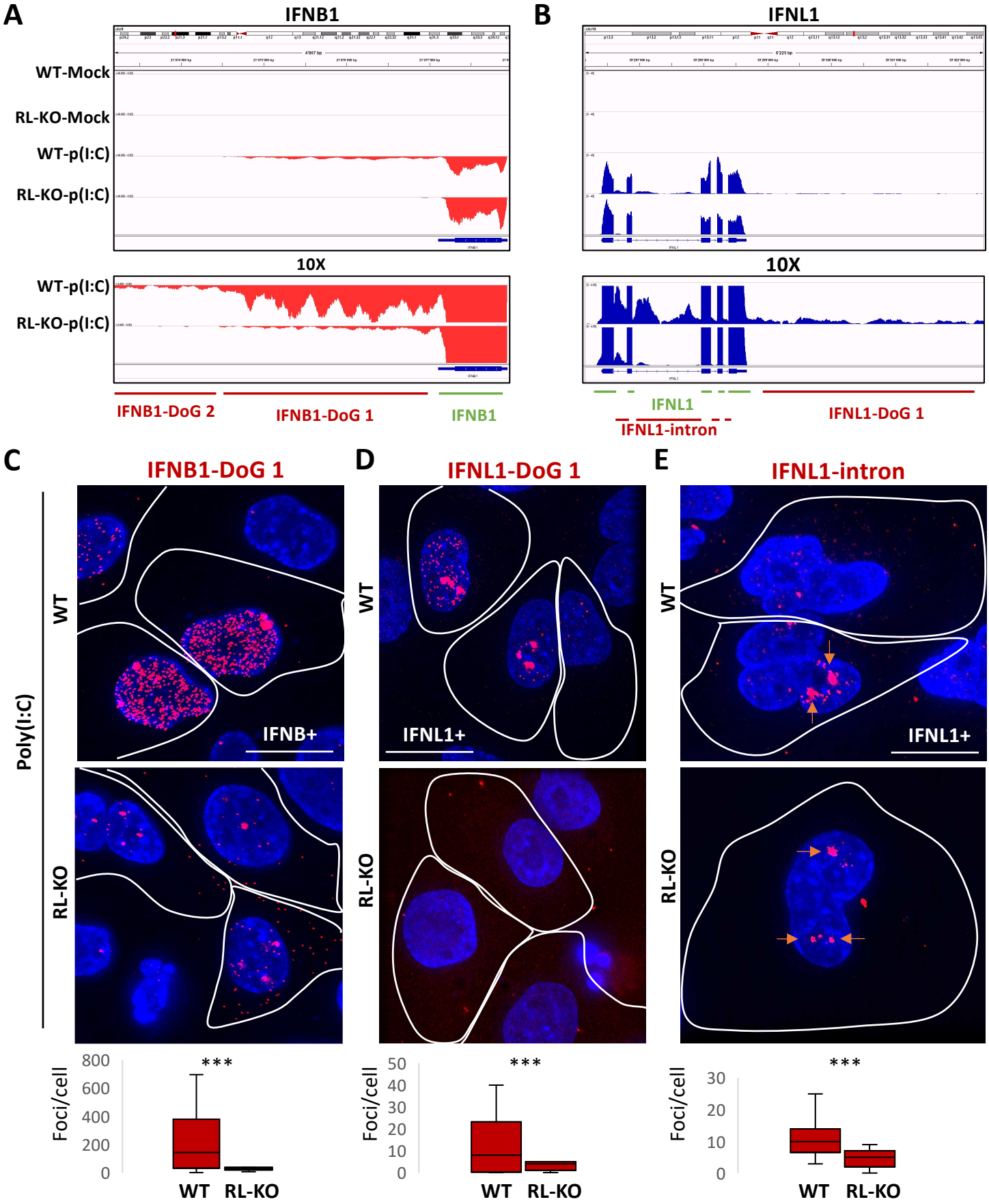
A
IFNB1
WT-Mock
RL-KO-Mock
WT-p(I:C)
RL-KO-p(I:C)
10X
WT-p(I:C)
RL-KO-p(I:C)
IFNB1-DoG 2
IFNB1-DoG 1
IFNB1
B
IFNL1
10X
IFNL1
IFNL1-intron
IFNL1-DoG 1
C
IFNB1-DoG 1
D
IFNL1-DoG 1
E
IFNL1-intron
Poly(I:C)
WT
RL-KO
IFNB+
IFNL1+
IFNL1+
Foci/cell
800
600
400
200
0
***
WT
RL-KO
50
40
30
20
10
0
30
20
10
0

Figure 5

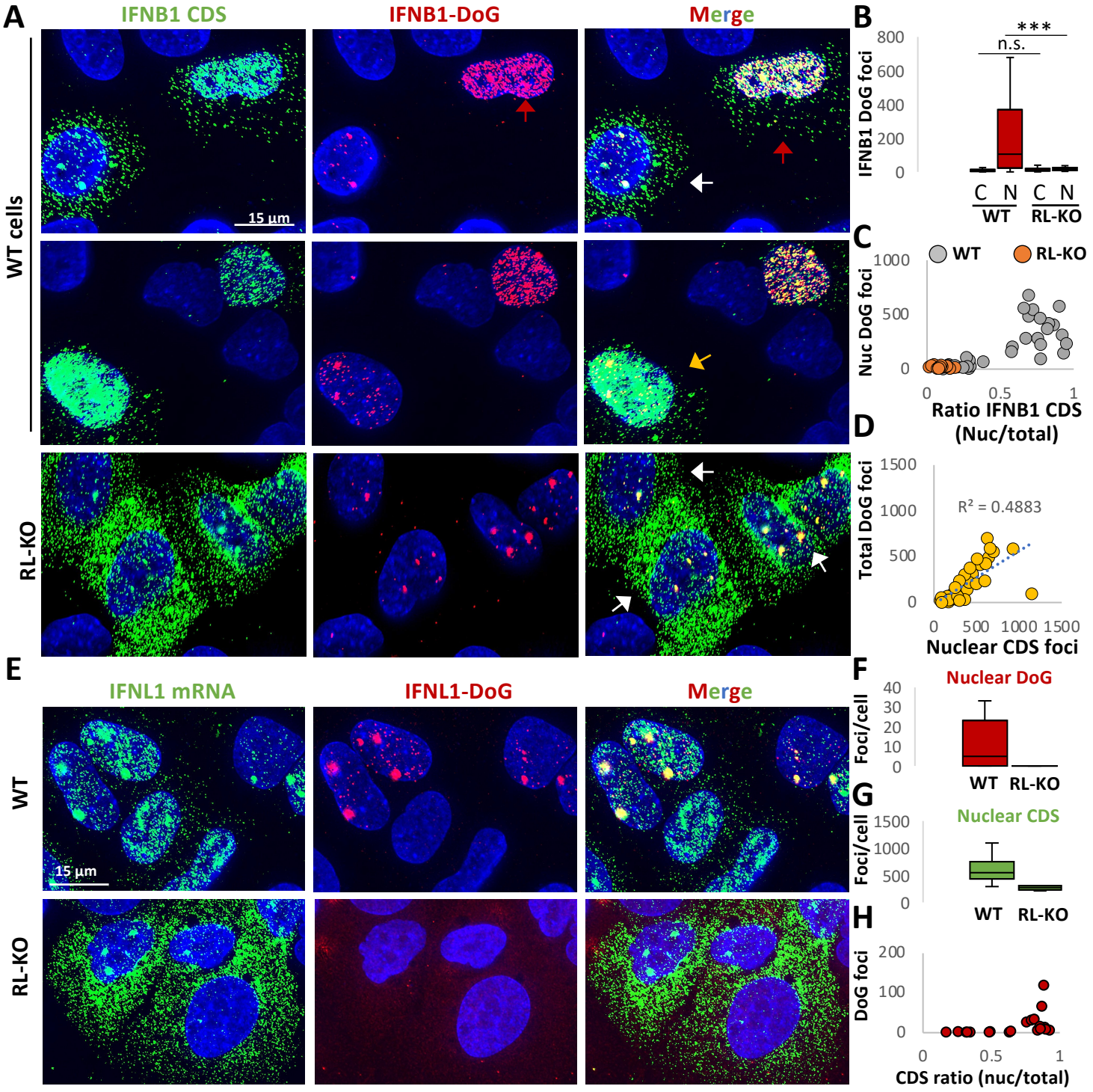
A
IFNB1 CDS
IFNB1-DoG
Merge
WT cells
RL-KO
15 µm
B
IFNB1 DoG foci
800
600
400
200
0
***
n.s.
C N C N
WT RL-KO
C
WT
RL-KO
Nuc DoG foci
1000
500
0
0 0.5 1
Ratio IFNB1 CDS (Nuc/total)
D
Total DoG foci
1500
1000
500
0
R² = 0.4883
0 500 1000 1500
Nuclear CDS foci
E
IFNL1 mRNA
IFNL1-DoG
Merge
WT
RL-KO
15 µm
F
Nuclear DoG
Foci/cell
40
30
20
10
0
WT RL-KO
G
Nuclear CDS
Foci/cell
1500
1000
500
0
WT RL-KO
H
DoG foci
200
100
0
0 0.5 1
CDS ratio (nuc/total)

Figure 6

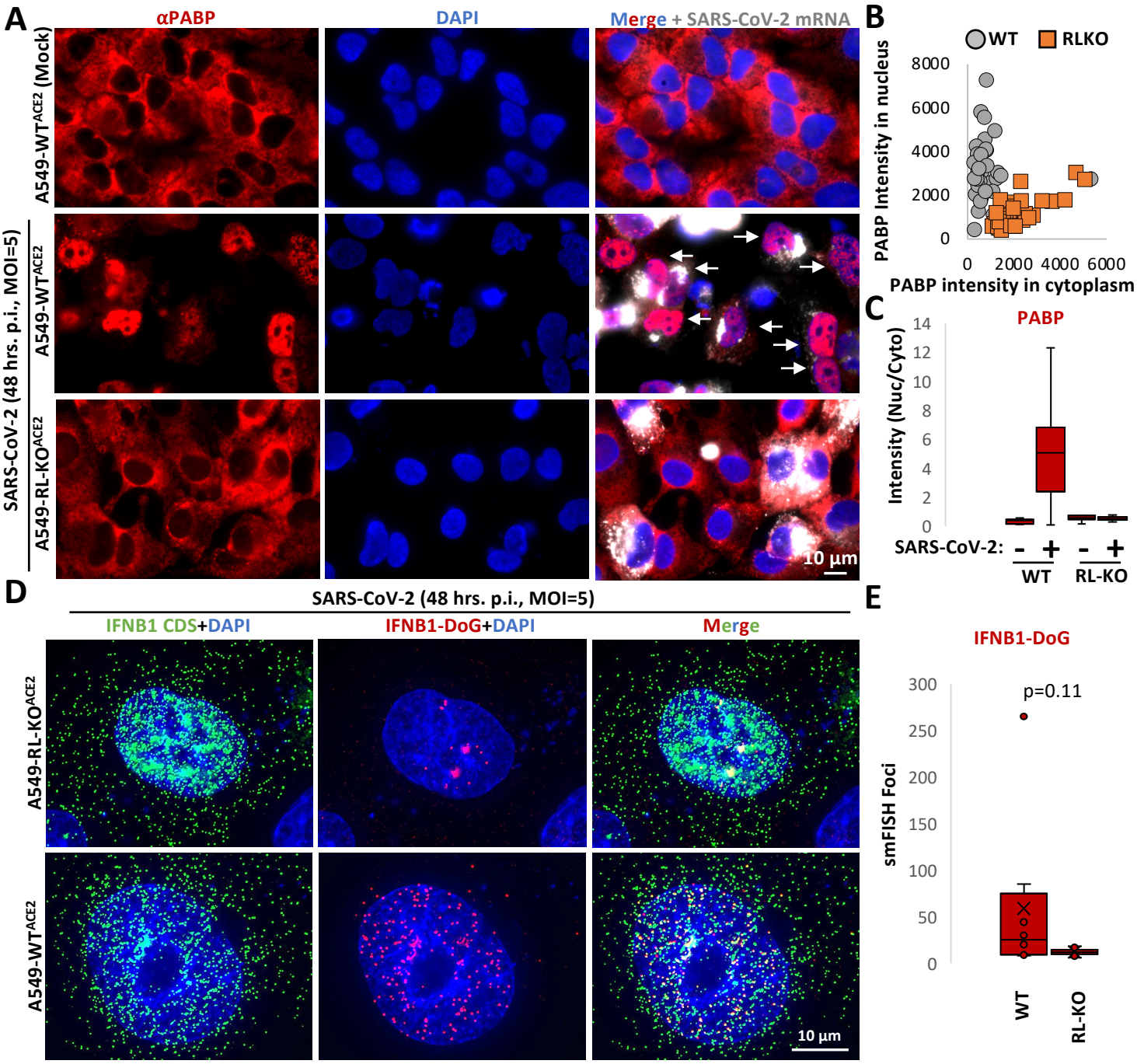
A
αPABP
DAPI
Merge + SARS-CoV-2 mRNA
A549-WT^ACE2 (Mock)
SARS-CoV-2 (48 hrs. p.i., MOI=5)
A549-WT^ACE2
A549-RL-KO^ACE2
10 µm
B
WT
RLKO
PABP Intensity in nucleus
PABP intensity in cytoplasm
C
PABP
Intensity (Nuc/Cyto)
SARS-CoV-2:
WT
RL-KO
D
SARS-CoV-2 (48 hrs. p.i., MOI=5)
IFNB1 CDS+DAPI
IFNB1-DoG+DAPI
Merge
A549-RL-KO^ACE2
A549-WT^ACE2
10 µm
E
IFNB1-DoG
p=0.11
smFISH Foci
WT
RL-KO

Figure 7

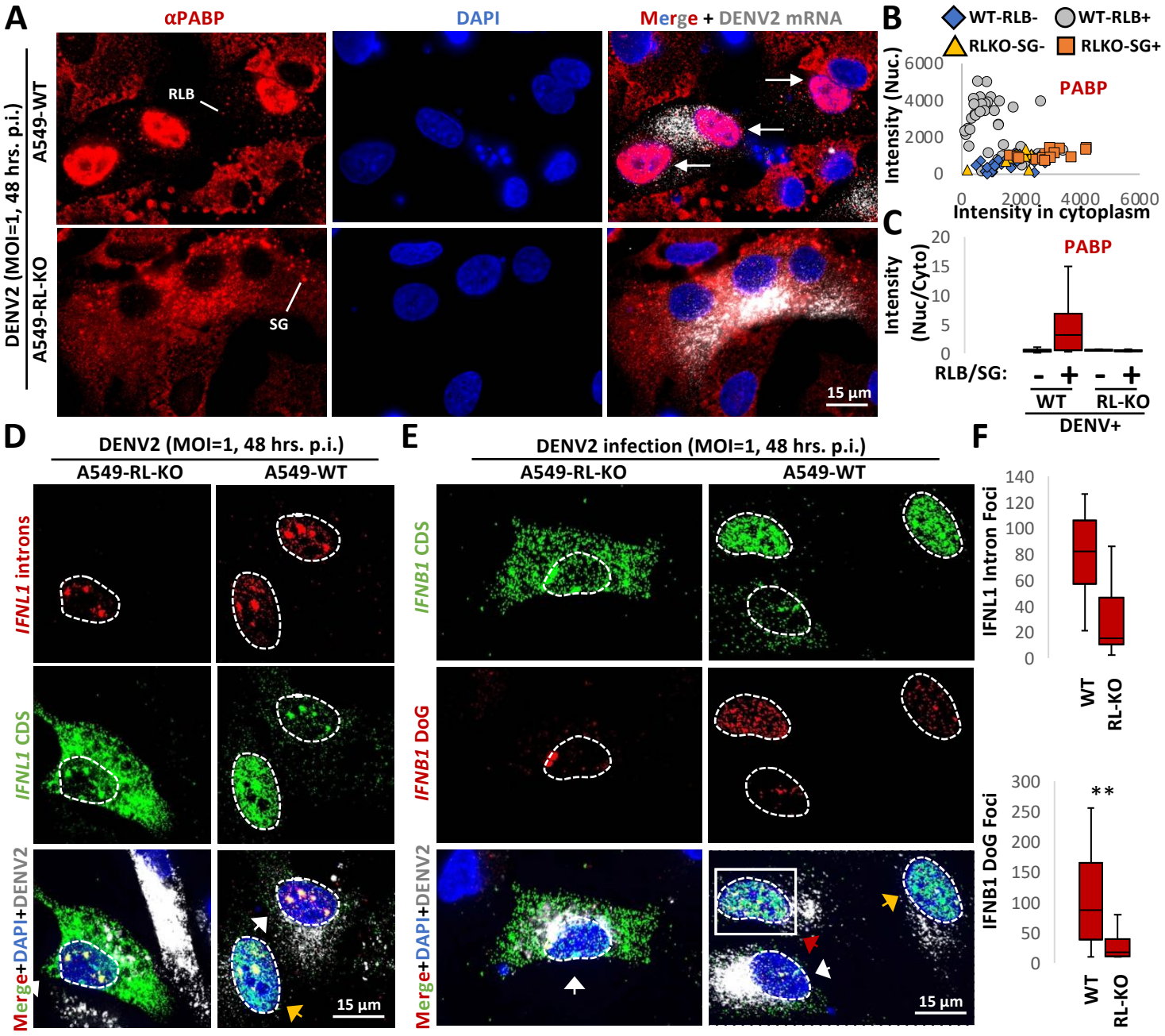
A
αPABP
DAPI
Merge + DENV2 mRNA
DENV2 (MOI=1, 48 hrs. p.i.)
A549-WT
A549-RL-KO
RLB
SG
15 µm
B
WT-RLB-
WT-RLB+
RLKO-SG-
RLKO-SG+
PABP
Intensity (Nuc.)
Intensity in cytoplasm
C
PABP
Intensity (Nuc/Cyto)
RLB/SG:
WT
RL-KO
DENV+
D
DENV2 (MOI=1, 48 hrs. p.i.)
A549-RL-KO
A549-WT
IFNL1 introns
IFNL1 CDS
Merge+DAPI+DENV2
15 µm
E
DENV2 infection (MOI=1, 48 hrs. p.i.)
A549-RL-KO
A549-WT
IFNB1 CDS
IFNB1 DoG
Merge+DAPI+DENV2
15 µm
F
IFNL1 Intron Foci
WT
RL-KO
IFNB1 DoG Foci
**
WT
RL-KO

Figure 8

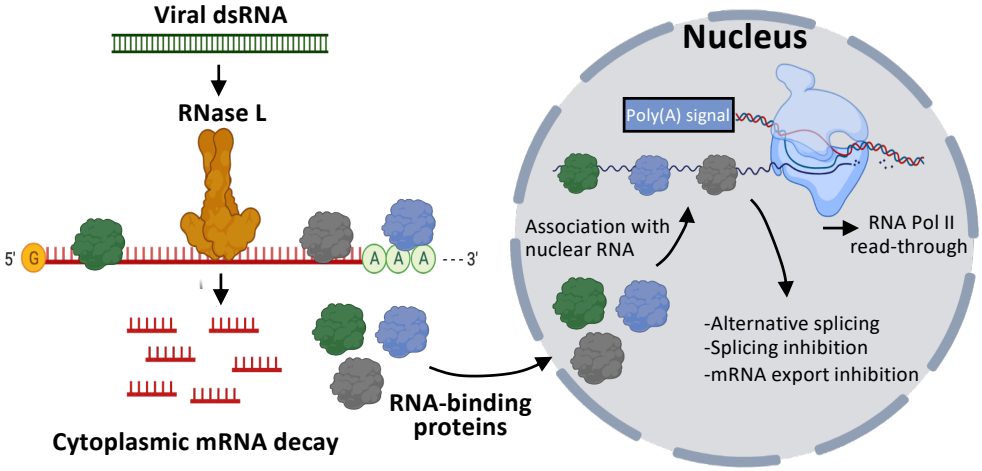
Viral dsRNA
RNase L
5'
G
A
A
A
---3'
Cytoplasmic mRNA decay
RNA-binding proteins
Nucleus
Poly(A) signal
Association with nuclear RNA
RNA Pol II read-through
-Alternative splicing
-Splicing inhibition
-mRNA export inhibition

Figure 9

748 **FIGURE LEGENDS**

749

750 **Fig. 1. RNase L-dependent accumulation of RBPs in the nucleus.**

751 (A) Immunofluorescence assay for PABP in wild-type (WT) or RNase L knockout (RL-KO) A549 cells
752 following four hours of lipofection with or without poly(I:C). (B) Immunofluorescence assay for RNA-
753 binding proteins that enrich in cytoplasmic stress granules. Dashed line represents the nuclear boundary as
754 determined by DAPI staining. (C) Quantification of the ratio (nucleus/cytoplasm) of the mean fluorescence
755 intensity.

756

757 **Fig. 2. Decay of RNAs specifically in the cytoplasm by RNase L results in nuclear accumulation of**
758 **RBPs.**

759 (A) FISH for poly(A)+ RNA and immunofluorescence assay for G3BP1 in WT and R-KO A549 cells. WT
760 cells with RNase L-dependent bodies (RLBs) or RL-KO cells containing stress granules (SGs) are indicated
761 by white arrows. Cells without RLBs or SGs are non-responsive (N.R.) and are indicated by yellow arrows.
762 (B) Quantification of poly(A)+ RNA signal in the nucleus (nuc.) or cytoplasm (cyto.) in WT and RL-KO
763 cells with or without RLBs or SGs, respectively, as represented in (A). (C) Immunoblot analysis of
764 endogenous RNase L in whole cell lysate (w), nuclear fraction (n), or cytoplasmic fraction (c) from A549-
765 WT cells. (D) Schematic showing RBP re-localization following either cytoplasmic RNase L activation
766 (left) or activation of nuclear-localized RNase L (RL-NLS). (E) Immunoblot for RNase L in whole cell (w),
767 nuclear (n), and cytoplasmic (c) crude fractions showing nuclear localization of the RNase L-NLS. (F)
768 Immunofluorescence assay for PABP and FISH for poly(A)+ RNA in parental A549 cells or A549 that
769 express RNase L-NLS construct following mock or poly(I:C) lipofection. (G) Quantification of PABP and
770 poly(A)+ RNA signal from (F).

771

772 **Fig. 3. RNase L activation results in alterations to alternative splicing.**

773 (A) Scatterplot comparing ΔPSI values in RL KO vs WT cells treated with poly(I:C) on the y axis and
774 WT control vs WT poly(I:C) treated cells on the x axis. The 140 splicing events shown are significant in
775 at least one comparison. Genes validated in panel C are labeled. (B) List of genes significant in both
776 comparisons from panel A. RBPs known to regulate splicing are shown in bold. (C) Validation of splicing
777 events by low cycle radiolabeled RT-PCR. The red asterisk in the PTBP1 gel is a nonspecific product.
778 Bar graphs show quantification of 4 biological replicates. * is $p < 0.05$, ** is $p < 0.01$, *** is $p < 0.001$,
779 *** is $p < 0.0001$

780

781 **Fig. 4. RNase L activation results in global alterations to host RNA processing.**

782 (A) Distribution of intron/exon ratios of host RNAs in WT and RL-KO cells following mock or poly(I:C)
783 lipofection. (B) Distribution of $DoG_{1\text{-}5000bp}$/exon ratios of host RNAs in WT and RL-KO cells following
784 mock or poly(I:C) lipofection. (C) IGV traces mapping to an example gene. Intron retention and DoG
785 formation is highlighted in WT cells following poly(I:C) lipofection.
786
787 **Fig. 5. RNase L promotes DoG transcriptional read-through and intron retention in type I and type**
788 **III interferon RNAs.**
789 (A) IGV traces mapping to IFNB1. Below shows the regions targeted by smFISH probes. (B) IGV traces
790 mapping to IFNL1. Below shows the regions targeted by smFISH probes. (C) smFISH for IFNB1-DoG
791 sixteen hours post-lipofection of poly(I:C) in WT and RL-KO cells. The cells that induced IFNB1, as
792 determined by smFISH for the CDS of IFNB1 (Fig. S4A,B), are demarcated by a white line. IFNB1 DoG
793 smFISH foci are quantified in WT an RL-KO cells in the graph below. (D and E) similar to (C) but for (D)
794 IFNL1-DoG-1 RNA sixteen hours post-lipofection of poly(I:C) or (E) IFNL1-intron RNA twelve hours
795 post-lipofection of poly(I:C). Staining and quantification of IFNL1 CDS is shown in Fig. S4C,D,E.
796
797 **Fig. 6. DoG RNA included on interferon-encoding mRNAs correlates with their nuclear retention.**
798 (A) Co-smFISH for the CDS and DoG-1 regions of IFNB1 sixteen hours post-lipofection of poly(I:C). (B)
799 Box plots displaying of the number of IFNB1-DoG foci localized to the nucleus (n) or cytoplasm (c) in WT
800 or RL-KO cells as represented in (A). (C) Scatter plot of the ratio (nucleus/cytoplasm) of IFNB1-CDS foci
801 (x-axis) and nuclear IFNB1-DoG foci (y-axis) show positive correlation between DoG RNA and nuclear
802 retention. (D) Scatter plots of the quantity of nuclear IFNB1-DoG foci (y-axis) and the quantity of nuclear
803 IFNB1-CDS foci shows IFNB1 DoG RNA increase as the absolute number of IFNB1 CDS smFISH in the
804 nucleus increases. (E) Co-smFISH for the CDS and DoG-1 regions of IFNL1 sixteen hours post-lipofection
805 of poly(I:C). (F and G) Quantification of (F) nuclear IFNL1-DoG-1 foci or (G) IFNL1-CDS foci as
806 represented in (E). (H) Scatterplot of the ratio (nucleus/cytoplasm) of IFNL1-CDS foci (x-axis) and nuclear
807 IFNL1-DoG foci (y-axis).
808
809 **Fig. 7. RNase L promotes nuclear RBP influx and DoG transcriptional read-through of IFNB1 during**
810 **SARS-CoV-2 infection.**
811 (A) Immunofluorescence assay for PABP in WT^{ACE2} and $RL\text{-}KO^{ACE2}$ A549 cells forty-eight hours post-
812 infection with SARS-CoV-2 (MOI=5) or mock-infected WT cells. To identify infected cells, smFISH for
813 SARS-CoV-2 ORF1b mRNA was performed. (B) Scatter plot of mean intensity values for PABP staining
814 in the nucleus (y-axis) or cytoplasm (x-axis) in mock or SARS-CoV-2-infected WT^{ACE2} or $RL\text{-}KO^{ACE2}$
815 A549 cells as represented in (A). Dots represent individual cells. (C) Box plot of the ratio

816 (nucleus/cytoplasm) of the mean intensity of PABP as represented in (A). (D) smFISH for IFNB1-CDS and
817 IFNB1-DoG forty-eight hours post-infection with SARS-CoV-2 in WT^{ACE2} or $RL\text{-}KO^{ACE2}$ A549 cells
818 (MOI=5). (E) Quantification of IFNB1 DoG RNA in WT and RL-KO cells.
819
820
821 **Fig. 8. RNase L promotes nuclear RBP influx and DoG transcriptional read-through and intron**
822 **retention during dengue virus infection.**
823 (A) Immunofluorescence assay for PABP in WT and RL-KO A549 cells infected with dengue virus
824 serotype 2 (DENV2) forty-eight hours post-infection (MOI=1). smFISH for DENV2 mRNA was performed
825 to identify infected cells. (B) Scatter plot of mean intensity values for PABP staining in WT or RL-KO cells
826 that did or did not activate the dsRNA response based on RLB assembly (WT cells) or SG assembly (RL-
827 KO) cells as represented in (A). (C) Box plot of the ratio (nucleus/cytoplasm) of the mean intensity of
828 PABP (B). (D) smFISH for IFNL1-CDS, IFNL1-intron, and DENV mRNA in WT or RL-KO cells forty-
829 eight hours post-infection with DENV2 (MOI=1). (E) smFISH for IFNB1-CDS and IFNB1-DoG in WT or
830 RL-KO cells forty-eight hours post-infection with DENV2 (MOI=1). (F) Box plots quantifying the smFISH
831 from (D and E).
832
833 **Fig. 9. Model for RNase L-mediated regulation of nuclear RNA processing.**
834 Activation of RNase L in response to viral double-stranded RNA (dsRNA) results decay of cytoplasmic
835 RNAs. RNA-binding proteins (RBPs) disassociate from degraded cytoplasmic RNA and shuttle to the
836 nucleus where they bind to nuclear RNA. The binding of RBPs to nuclear RNA alters RNA processing
837 events.